

Soft Materials Architectures for Robot Manipulation

Ryan Coulson

CMU-RI-TR-20-42

August 2020

School of Computer Science
Carnegie Mellon University
Pittsburgh, PA 15213

Thesis Committee:

Carmel Majidi (Chair)

Nancy Pollard

Ankit Bhatia

*Submitted in partial fulfillment of the requirements
for the degree of Master of Science.*

Copyright © 2020 Ryan Coulson

Abstract

Robot manipulation has been a prolific subject of academic research for several decades - however, today's robotic manipulators have yet to demonstrate an ability to perform robust and versatile dexterous manipulation. This challenge can largely be attributed to a trade-off between complexity and capability in the design of robotic manipulators. In order to bridge this gap, we leverage the paradigm of Soft Robotics. This work involves the development of two distinct soft robotic end effectors. The first is a stiffness and adhesion tuning gripper, which is capable of grasping objects of various shapes, weights, and sizes. Pull-off tests conducted using this gripper show that transitioning from a soft to stiff state during grasping enables up to $6\times$ increase in adhesion strength. The second end effector developed for this study is a tendon driven foam hand, which is intended to be highly dexterous while requiring a low number of motors for actuation. We develop a hand which demonstrates a high potential for dexterity, and indicate a design based on postural synergies which would allow it to complete 5 distinct dexterous tasks using only two motors.

Acknowledgments

Lots of people to thank here.

First of all, thanks to my advisor Carmel, for guiding me through my two years of research at CMU.

Also, thanks to Nancy Pollard and Abhinav Gupta, who fulfilled additional advisory roles for the foam hand project.

Thanks to all of the individuals who have helped me with my research along the way. To Steven Rich, for getting me started with the thermoplastic composite. To Mo Malakooti, for helping me collect the DMA data. To Zeyu Yan, for helping me figure out how to fabricate flexible heaters. To Kevin Turner and Chris Stabile for implementing the finite element model for the soft gripper. To Dominik Bauer, Jonathan King, and Ella Moore, for sharing their knowledge on the design of foam hands. And to Karmesh Yadav, for working with my foam hand prototypes to try controlling them using reinforcement learning.

A big thanks to every member of the Soft Machines Lab - almost all of you have helped me in one way or another at some point in the last two years.

Thanks to my thesis committee: Carmel, Nancy, and Ankit Bhatia.

Thanks to my friends, especially the “Foozin Squad” - Anish, Eric, Josh, Vai, and Will - for helping to keep me grounded during my time at CMU.

And finally, thanks to my parents, who have provided their unwavering support throughout the whole journey.

Contents

1	Introduction	1
1.1	Robot Manipulation	1
1.2	Soft Robotic End Effectors	2
1.3	Contribution	4
2	Stiffness & Adhesion Tuning Soft Gripper	5
2.1	Background	5
2.2	Methodology	6
2.2.1	Material Selection, Synthesis, & Characterization	6
2.2.2	Gripper Design	6
2.2.3	Experimental Setup	11
2.2.4	Finite Element Model	11
2.3	Results and Discussion	14
2.3.1	Pull-off Testing	14
2.3.2	Comparison of FEA and Experimental Results	17
2.3.3	Pick-and-place Demonstrations	18
2.3.4	Limitations	19
2.4	Concluding Remarks	20
3	Design Optimization of a Tendon Driven Foam Hand	21
3.1	Background	21
3.2	Methodology	23
3.2.1	Evaluating Dexterity	23
3.2.2	Morphology	25
3.2.3	Tendon Routing	26
3.2.4	Postural Synergies	28
3.3	Results and Discussion	31
3.3.1	Fully Actuated Hand	31
3.3.2	Software Synergies	32
3.3.3	Limitations	34
3.4	Concluding Remarks	36

4	Conclusions and Future Work	37
A	Criteria for Manipulation Patterns	39
B	Photo Sequences of Manipulation Patterns	41
C	Low Dimensional Reconstructions of Data	45
D	Dimensioned Drawing of Foam Hand Prototype	47

List of Figures

1.1	Line drawing of the Utah/MIT Hand [1].	2
1.2	(a) Universal gripper [2]. (b) SDM Hand [3]. (c) RBO Hand II [4]. (d) Gecko gripper [5].	3
2.1	(A) Fully integrated robotic system, with gripper mounted to robot arm. (B) Gripper with contact pad attached. (C) Contact pad containing a stiffness tuning element composed of carbon-filled polycaprolactone (PCL) composite and serpentine copper heater.	7
2.2	Results from DMA test of PCL composite with PCL of molecular weight 88.4 kg mol^{-1} and 20% loading fraction of carbon black.	8
2.3	(a) Fabrication process: (i) Copper-clad polyimide is laminated to a PDMS bed, with polyimide facing upwards. (ii) Copper-clad polyimide is machined by ultra-violet laser. (iii) Excess copper-clad polyimide is removed from the PDMS bed, leaving only the serpentine traces. Traces are then laminated to VHB tape and removed from the bed. (iv) Traces and VHB tape (i.e. flexible heater) are placed on top of the composite, with copper facing upwards, and adhered to the surface using a hand iron. Wires are then soldered to connection points on the traces. (v) Stiffness tuning element is placed inside of the mold, on top of a $500 \mu\text{m}$ thick layer of silicone. Mold is filled with silicone and placed in a 70°C oven to cure for 30 minutes. (vi) Mold is removed from the oven and the contact pad is separated from the mold. (b) Exploded view of contact pad. Thickness of the bottom layer of silicone is $500 \mu\text{m}$. Thickness of the composite is 1.5 mm. Thickness of the top layer of silicone is 1 mm. Total thickness of the contact pad is 3 mm.	9

2.4	(A) Pull-off testing procedure for state = stiff: (1) Initially, the contact pad is in its soft state, with the bottom edge several millimeters above the acrylic substrate. Then, the Instron crosshead begins moving downwards. (2) Contact pad comes into contact with the substrate. (3) The crosshead reaches its resting height and stops moving. (4) Contact pad is allowed to rest on the substrate for 5 minutes. During this time, stress relaxation occurs due to the viscoelasticity of the composite. (5) Crosshead begins retracting. (6) The pad loses contact with the substrate. Afterwards, the crosshead continues moving upwards until it reaches its starting height. (B) Pull-off testing procedure for state = soft. This is identical to the stiff state procedure except for heating of the contact pad. The plots and images shown correspond to tests with parameters, $S = 46$ mm, and $H = 17.5$ mm on a flat substrate. (C) State = stiff and state = soft loading cycles overlaid. (D) Parameters controlling contact pad geometry. S is the distance between the gripper's jaws and H is the distance between the bottom of the gripper jaws and the top of the acrylic substrate.	12
2.5	(A) Finite element schematic of the initial flat state. (B) Finite element deformation process showing (i) the initial flat state, (ii) application of gravity, (iii) compression, and (iv) contact formation.	13
2.6	Pull-off test results for the flat substrate: (a) Superimposed loading cycles from consecutive trials with parameters state = stiff, $S = 46$ mm, $H = 17.5$ mm. (b) Superimposed loading cycles from consecutive trials with parameters state = soft, $S = 46$ mm, $H = 17.5$ mm. (c) Representative photograph, $S = 37$ mm, $H = 15$ mm. (d) Averaged results for tests with condition state = stiff. (e) Averaged results for tests with condition state = soft. (f) Ratio of pull-off force between stiff and soft conditions.	15
2.7	Pull-off test results for the cylindrical substrate: (a) Superimposed loading cycles from consecutive trials with parameters state = stiff, $S = 51$ mm, $H = -18$ mm. (b) Superimposed loading cycles from consecutive trials with parameters state = soft, $S = 51$ mm, $H = -18$ mm. (c) Representative photograph, $S = 51$ mm, $H = -5$ mm. (d) Averaged results, S held constant at 51 mm.	16
2.8	Deformed profiles of the contact pad prior to retraction. Predictions from FEA with logarithmic maximum principal strain contours are shown in the left column, and experimental results are shown in the right column.	18
2.9	Grasping various objects: (A) Playing card, 1.62 g. (B) Silicon wafer, 9.38 g. (C) Small tomato, 25.3 g. (D) Juice can, 36.6 g.	18
3.1	(a) CAD images of the foam hand prototype. (b) CAD model of the multi-part mold used to fabricate the foam hand.	25
3.2	Coordinate axes for a human hand (left) and the foam hand prototype (right). . . .	26
3.3	Diagram illustrating how a foam finger can be actuated with four tendons in a way that allows it to bend in any direction.	26

3.4	Diagram illustrating fingertip workspaces. The workspace is the area <i>between</i> dotted lines. (left) Finger actuated by individual tendons running along its length. (right) Finger actuated by multiple tendons (proximal and distal) running along its length.	27
3.5	Tendon routing diagram for the final foam hand prototype.	27
3.6	Comparisons between human and robot postures: RockII (top) and Palmar Slide (bottom).	31
3.7	Scree plot for principal component analysis using only data from successfully completed manipulation patterns as input.	33
3.8	(a) Two-dimensional reconstruction of manipulation patterns. (b) Hand postures corresponding to minimum, maximum, and centroid values for PC1 and PC2. . . .	35
3.9	Hand postures corresponding to minimum and maximum values of higher order principal components.	36
C.1	Two-dimensional reconstructions of manipulation patterns for: (top) successful subset, and (bottom) all data. Clusters not common to both plots are circled in blue.	46
D.1	Dimensions in millimeters. The radius of the base of each finger is 11 mm and the radius of the fingertips is 11 mm. The radius of the mid-line of the index and middle fingers is 50 mm (arc length 79 mm). The radius of the midline of the thumb is 40 mm (arc length 62 mm).	47

List of Tables

3.1	Number of principal components required to complete each manipulation pattern. The “Subset” column applies to principal components which were derived using only data from manipulations which were successfully completed by the fully actuated hand. The “All Column” refers to principal components which were derived using the full dataset.	33
3.2	Number manipulations successfully completed versus number of principal components applied. The “Subset” column applies to principal components which were derived using only data from manipulations which were successfully completed by the fully actuated hand. The “All Column” refers to principal components which were derived using the full dataset.	33

Chapter 1

Introduction

1.1 Robot Manipulation

Robot manipulation has been an important and highly studied topic of research for many years. Robotic manipulators (grippers, hands, end effectors) have a range of applications, from industrial robotics to prosthetics to human-robot interaction [6]. Although many robust manipulation solutions have been developed for use outside of laboratory settings, there are still several key challenges associated with robot manipulation. In this paper, we will focus on limitations related to hardware design.

With regard to the design of hardware for robot manipulation, there is a fundamental trade-off between complexity and capability. Perhaps the simplest of these designs are 2-fingered parallel-plate grippers, which are also some of the most common designs used both in research and industry. These grippers are highly favored for many applications because they are exceptionally easy to program and control, and therefore present a very low barrier to usage. Despite their simple design, these grippers are capable of performing a wide range of tasks. However, for complicated manipulation tasks, more versatile end effectors may be required.

The need for more versatile end effectors motivated the development of multi-fingered robotic hands - inspired by the human hand - which began in earnest in the 1980's with seminal work such as the Stanford/JPL Hand [7] and Utah/MIT Hand [1] (see Figure 1.1). These robotic hands had complex mechanical designs (relative to parallel grippers) which incorporated a high number of degrees of freedom (9 for the Stanford/JPL Hand and 16 for the Utah/MIT Hand), theoretically enabling high levels of versatility and dexterity. However, due to the correspondingly high degrees of actuation (12 for the Standord/JPL Hand and 32 for the Utah/MIT Hand), control of these hands was extremely difficult, which severely limited their efficacy.

Since the development of these early robotic hands, an extraordinary number of novel designs for robotic end effectors has followed [6]. However, despite this terrific level of innovation, the challenges of robot manipulation today are still largely the same as they were in the 1980's [8].

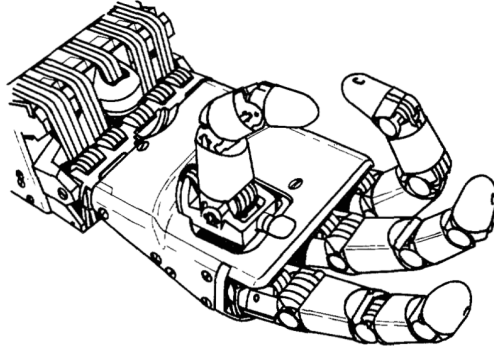


Figure 1.1: Line drawing of the Utah/MIT Hand [1].

Specifically, the trade-off between capability and complexity in mechanical design remains highly relevant, as modern robotic end effectors have yet to demonstrate an ability to perform robust and versatile dexterous manipulation.

1.2 Soft Robotic End Effectors

One paradigm which may offer a solution to this trade-off between complexity and capability in the design of robotic manipulators is that of soft robotics [9]. The guiding principle of soft robotics is that by incorporating soft materials - such as silicone rubbers - into the design of robotic systems, improvements in performance can be realized while reducing the need for sensorization and complex control algorithms. This is possible primarily due to the compliance of soft materials, which allows them to conform and adapt to their environments. Compliance enables an element of “embodied intelligence” [10] in soft robotic systems, which is to say that the adaptability of the robot’s physical structure offloads some of the computation which is normally handled via sensing and control.

In order to better understand the advantages of soft robotic systems, we can consider several seminal examples of soft robotic end effectors as case studies - namely, the “Universal” Gripper [2, 11], the Shape Deposition Manufacturing (SDM) Hand [3], the RBO Hand 2 [4], and the Gecko Gripper [5] (see Figure 1.2).

The Universal Gripper consists quite simply of a rubber membrane filled with a granular material (e.g. a latex balloon filled with coffee grounds), connected to an air pump. This gripper is highly compliant - thus, when it is pressed into contact with an object, it conforms to the object’s surface, effectively enveloping it. Once the gripper has established intimate contact with an object, the air pump is used to extract air from the gripper, creating a vacuum within the rubber membrane. This results in a phenomenon known as granular jamming, where the granular particles inside of the gripper’s rubber membrane are packed together, which leads to a dramatic increase in the overall stiffness of the system. In this manner, the gripper is able to “lock in” its adaptive shape, allowing it to maintain intimate contact with the object while lifting it. When air is restored to the gripper, it returns to its original compliant state and the object is released. This gripper is capable

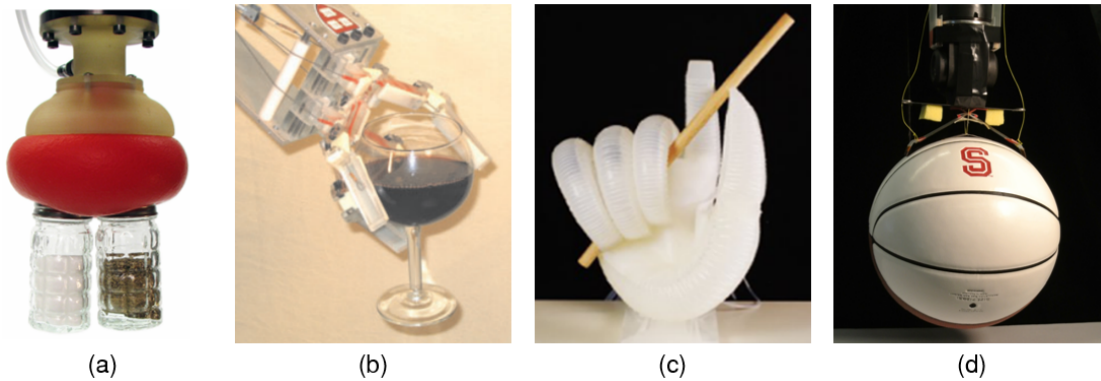


Figure 1.2: (a) Universal gripper [2]. (b) SDM Hand [3]. (c) RBO Hand II [4]. (d) Gecko gripper [5].

of robustly grasping objects spanning a wide range of geometries without the need for any sensors or a sophisticated control strategy. Additionally, due to its compliance it is able to grasp delicate objects without any risk of causing damage.

The SDM Hand is a multi-fingered gripper with fingers consisting of rigid plastic links, connected by flexible urethane joints. The design principle of the SDM Hand is simple: its flexible joints allow it to adapt to the shape of objects being grasped while requiring only one actuator. It demonstrates that effective soft robotic systems can be designed without the need for the entire robot to be made of soft materials.

The RBO Hand 2 is an anthropomorphic hand which uses silicone-based pneumatic actuators as fingers. This hand has the same grasp adaptivity benefits as the SDM Hand; additionally, due to its anthropomorphic design and high number of degrees of freedom (technically infinite), it is capable of more complex manipulation tasks. This hand uses 7 actuators, which gives it a lower actuation dimensionality than most high-DoF robotic hands.

The Gecko Gripper is inspired by gecko feet and achieves reversible adhesion using silicone microfibers which generate a van der Waals force between the gripper and the object. This gripper demonstrates that soft materials can also enable adhesion-based grasping, in addition to force closure-based grasping.

Despite all of the advantages of soft robotic end effectors, it is important to note that they also have limitations - such as a relative lack of durability, repeatability, and precision - which have largely excluded them from use outside of laboratory settings. As a final case study, consider the Amazon Picking Challenge [12] - an international competition challenging teams to design autonomous robotic systems capable of picking items from warehouse shelves - which has been won by suction cups and parallel-plate grippers in every year that it has been held. This demonstrates that simplistic robotic end effectors are the preferred option for leading researchers around the world, and suggests that soft robotic end effectors and complex mechanical hands alike still require substantial improvements before they can truly begin to outperform these simple alternatives.

1.3 Contribution

The contribution of this work is the development of two separate soft robotic end effectors meant to address some of the challenges faced by typical robot manipulators.

The first of these end effectors is a versatile stiffness and adhesion tuning gripper. Importantly, this gripper is capable of grasping simple convex objects *as well as* flat, low-profile objects such as playing cards and silicon wafers. Grasping flat objects is challenging for most grippers which rely upon force-closure-based grasping, while grasping non-flat objects can be challenging for adhesion-based grippers. As a result, developing grippers which are capable of robustly grasping both classes of objects is an open problem. While this gripper serves primarily as a simple proof-of-concept, we believe that it represents a significant milestone in the development of versatile adhesion-based grippers.

The second end effector described in this paper is a tendon driven foam hand. The design of this hand builds on previous work from King et al. [13]. The goal of this work was to optimize the design of the hand such that it demonstrated high levels of dexterity while requiring a low number of actuators in order to simplify control and reduce size, weight, and cost. We develop a hand which demonstrates a high potential for dexterity, and conduct a preliminary investigation into design strategies which may enable the hand to operate effectively using a low number of actuators. The mechanical implementation of these design strategies remains for future work.

Chapter 2

Stiffness & Adhesion Tuning Soft Gripper ¹

2.1 Background

Stiffness tuning - the ability of a material or system to transition between a soft, conformable state and a rigid, load bearing state - is an aspect of robotics that has received considerable attention in recent years. This is especially true within the field of soft robotics, where many different approaches have been developed to enable stiffness tuning for various applications [9, 14, 15]. Generally, these approaches can be grouped into one of four different categories: (1) granular jamming [2, 11, 16–18]; (2) electro- and magnetorheological materials [19, 20]; (3) shape memory polymers [21–27]; and (4) low melting point materials, e.g. waxes [28, 29], polymers [30–37], and metal alloys [38–41]. While the references provided above are generally relevant to this paper, they represent only a fraction of all of the research on stiffness tuning for soft robotics; for a more thorough review, see [9, 14, 15].

The work presented in this paper focuses on the use of a low melting point polymer (LMPP) for robotic grasping applications. The stiffness tuning principle of LMPPs is simple: these materials are stiff at room temperature (Young’s modulus > 10 MPa), and they soften as their temperature increases, ultimately undergoing a phase change that results in a soft “melt” state. Previously, several robotic grippers have been developed using LMPPs as an enabling material, including multi-fingered grippers with stiffness tuning ligaments or joints made of conductive propylene-based elastomer (cPBE) [35] and acrylate-based thermoplastic polymer (ATPP) [30], as well as silicone posts with stiffness tuning cores made of cPBE [36], which enabled tunable adhesion. However, while these grippers demonstrated the potential of LMPPs to aid in robotic grasping, their ability to effectively grasp a wide range of objects was limited. The goal of this research is to introduce an LMPP-based materials architecture and gripper design that allows for more versatile soft robot grasping.

The gripper described in this paper (see Figure 2.1) achieves tunable adhesion by controlling the

¹Ryan Coulson, Christopher J. Stabile, Kevin T. Turner, and Carmel Majidi. Versatile Soft Robot Gripper Enabled by Stiffness and Adhesion Tuning via Thermoplastic Composite. *Soft Robotics*. Submitted for publication, May 2020.

stiffness of a stiffness tuning element embedded within a silicone matrix, similarly to the device described in [36]. In adhesion-based grasping, the maximum adhesion force (also referred to as pull-off force) between the gripper and a target object determines the load capacity of the gripper. As a result, pull-off force is often used as a metric for evaluating the efficacy of adhesion-based grippers [28, 42–44]. To test the effectiveness of our gripper and help guide its future design, we conduct experiments to measure pull-off force as a function of various parameters. Additionally, a finite element model is developed to simulate the behavior of the gripper. Finally, the gripper is used for pick-and-place demonstrations with various objects.

2.2 Methodology

2.2.1 Material Selection, Synthesis, & Characterization

The LMPP chosen as the stiffness tuning element for this gripper was a thermoplastic composite consisting of polycaprolactone (PCL) loaded with carbon black. The process for synthesizing the composite is described in detail by Rich et. al [37]. Qualitative testing revealed that the most favorable composition was an 80:20 ratio of PCL (Perstorp AB) to carbon black (Alfa Aesar) by weight. The selected PCL had a molecular weight of 88.4 kg mol^{-1} (CAPA 6800).

As the composite’s loading fraction of carbon black increases, its stiffness at room temperature increases while its ductility decreases. Similarly, reductions in the molecular weight of PCL lead to increased stiffness and reduced ductility. We desired a composite that was maximally stiff at room temperature without being susceptible to fracture, and we found that the composite described above yielded the best results. An additional consideration was the viscosity of the composite in its melt state, which increases with molecular weight and loading fraction of carbon black. We required that the viscosity would be high enough that the composite would maintain structure in its melt state in order to support the embedded heater (described in subsequent sections). This requirement was also satisfied by the selected composition.

In order to characterize the stiffness tuning capabilities of the composite, we conducted a dynamic mechanical analysis (DMA) test with tensile loading. Results are shown in Figure 2.2. Testing revealed that the composite is mechanically stiff below $\sim 50^\circ\text{C}$, undergoes a phase change between 50°C and 67°C , and is soft above $\sim 67^\circ\text{C}$. Here, the storage modulus serves as a proxy for the Young’s modulus. The maximum switching ratio (i.e. the ratio of the moduli between stiff and soft states) for the composite is $\sim 300\times$, which is sufficiently high for most stiffness tuning applications [14, 15].

2.2.2 Gripper Design

The composite is loaded with carbon black, making it electrically conductive. Therefore, it is possible to heat the composite via Joule heating by attaching electrodes and running electrical current directly through the composite [37]. An ability to heat the composite is necessary because increasing temperature enables phase change. However, during preliminary testing, we found this

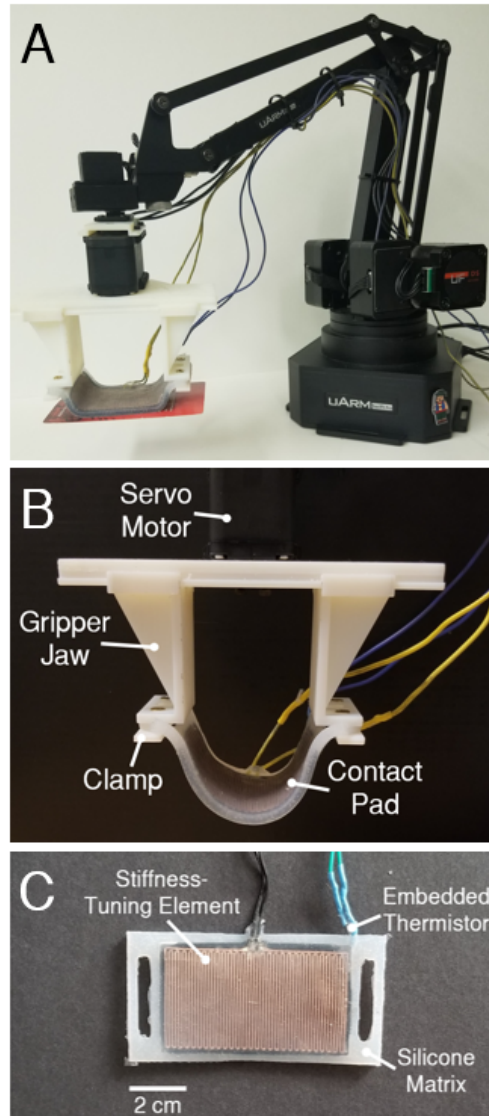


Figure 2.1: (A) Fully integrated robotic system, with gripper mounted to robot arm. (B) Gripper with contact pad attached. (C) Contact pad containing a stiffness tuning element composed of carbon-filled polycaprolactone (PCL) composite and serpentine copper heater.

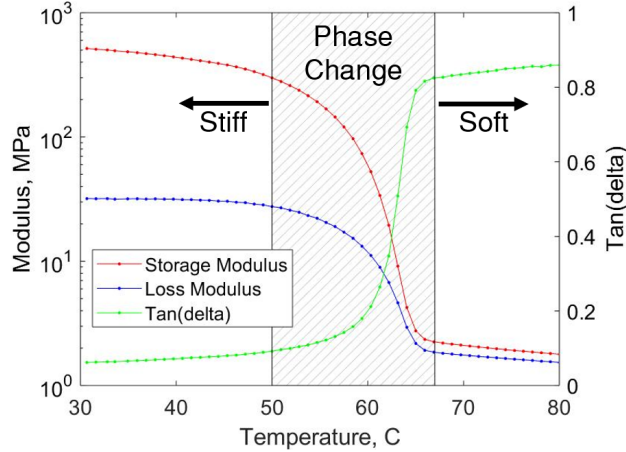


Figure 2.2: Results from DMA test of PCL composite with PCL of molecular weight 88.4 kg mol^{-1} and 20% loading fraction of carbon black.

method of direct Joule heating to be unreliable. The primary issue with direct Joule heating was that any variations in the cross-section of the composite would result in the formation of “hot spots,” or areas of localized heating. This is because the resistance of the composite at any location is inversely proportional to its cross-sectional area. Thus, in locations where the cross-sectional area was smaller than the nominal cross-sectional area, the resistance of the composite was high, resulting in a greater generation of thermal energy for the same amount of current. The problem with this localized heating was that it would not allow the composite to bend uniformly when subjected to external forces, and therefore did not meet the requirements for our application.

In order to apply uniform heat to the composite, we developed flexible resistance heaters by cutting serpentine copper traces, following the process established in [45, 46]. This process is depicted in Figure 2.3a. First, a $70 \mu\text{m}$ thick layer of flexible copper-clad polyimide (Pyralux FR8510R, DuPont) was laminated onto a PDMS bed (10:1 Sylgard 184, Dow Corning) with a rigid aluminum backing and cut using an ultraviolet laser (Protolaser U3, LPKF), as in [46]. The width of the traces was 0.6 mm. Then, a $51 \mu\text{m}$ thick layer of adhesive transfer tape (VHB F9460PC, 3M) was laminated to the traces, and the traces and tape were pulled away from the PDMS bed as a single unit, which we refer to as a flexible heater. The heater was then placed on top of a $70 \text{ mm} \times 40 \text{ mm}$, 1.5 mm thick rectangular piece of PCL composite, and was adhered to the composite using a hand iron. Thus, by running electrical current through the heater’s copper traces, heat is generated which is then distributed through the composite via thermal conduction. The result is that the entire composite can be heated to a nearly uniform temperature. Together, the flexible heater and PCL composite form the stiffness tuning element of the gripper.

After soldering wires to the flexible heater, the stiffness tuning element is embedded in a silicone matrix. The result is a “contact pad,” shown in Figures 2.1C and 2.3b. The first step of this process is creating a primary mold for the silicone matrix, shown in Figure 2.3a. This mold is made of VeroWhite (Stratays) and is fabricated using an Objet 3D printer (Stratasys). A separate mold is also fabricated using the same material which enables casting of a $70 \text{ mm} \times 40 \text{ mm}$ layer of silicone

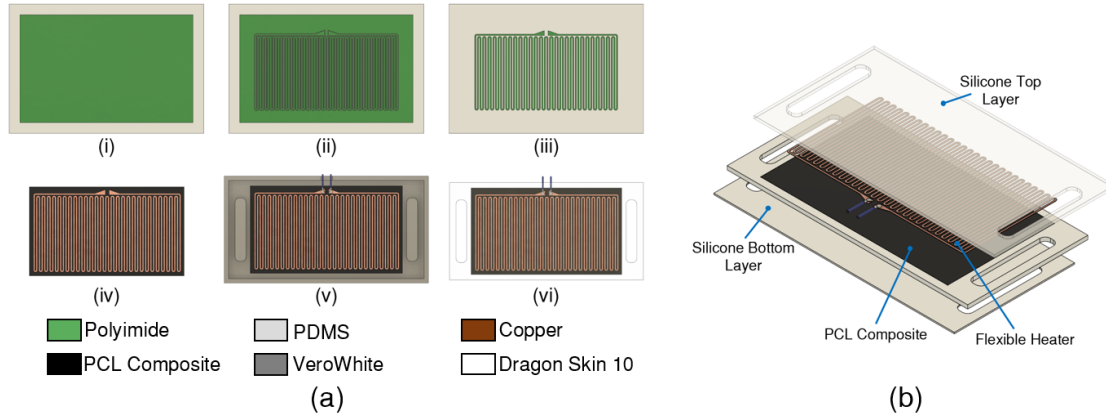


Figure 2.3: **(a)** Fabrication process: (i) Copper-clad polyimide is laminated to a PDMS bed, with polyimide facing upwards. (ii) Copper-clad polyimide is machined by ultraviolet laser. (iii) Excess copper-clad polyimide is removed from the PDMS bed, leaving only the serpentine traces. Traces are then laminated to VHB tape and removed from the bed. (iv) Traces and VHB tape (i.e. flexible heater) are placed on top of the composite, with copper facing upwards, and adhered to the surface using a hand iron. Wires are then soldered to connection points on the traces. (v) Stiffness tuning element is placed inside of the mold, on top of a 500 μm thick layer of silicone. Mold is filled with silicone and placed in a 70 $^{\circ}\text{C}$ oven to cure for 30 minutes. (vi) Mold is removed from the oven and the contact pad is separated from the mold. **(b)** Exploded view of contact pad. Thickness of the bottom layer of silicone is 500 μm . Thickness of the composite is 1.5 mm. Thickness of the top layer of silicone is 1 mm. Total thickness of the contact pad is 3 mm.

(Dragon Skin 10, Smooth-On) with a thickness of 500 μm . This layer of silicone is placed at the bottom of the primary mold and serves as the interface between the contact pad and target objects. It is important that this layer is cast in a dedicated mold in order to ensure consistent thickness, since its thickness will impact the overall adhesion strength of the contact pad [36]. Next, a thin layer of uncured silicone (Dragon Skin 10) is poured into the mold, and the stiffness tuning element is placed on top and pressed into contact with the cured layer of silicone beneath. Pouring uncured silicone into the mold before inserting the stiffness tuning element helps to ensure that any cavities on the bottom surface of the composite are filled with silicone, which prevents the formation of air pockets between the composite and the silicone matrix. Finally, the rest of the mold is filled with silicone, and the mold is placed in an oven set to 70 $^{\circ}\text{C}$ and left to cure for 30 minutes. The mold is then removed from the oven, and the contact pad is separated from the mold and left to cool.

Embedding the stiffness tuning element in a silicone matrix is important for several reasons. First, the silicone matrix helps the stiffness tuning element to maintain its structure. This is necessary because the PCL composite does not exhibit an elastic restoring force in its soft state. A helpful analogy is that the consistency of the composite in its soft state is similar to that of peanut butter. Thus, any deformation to the composite will be maintained in the absence of external forces. This characteristic is problematic because uniform heating of the composite is dependent upon the composite maintaining its original dimensions. Embedding the stiffness tuning element in a silicone matrix solves this problem since the original shape can be restored by the elasticity of the silicone. An additional benefit of the silicone matrix is that it allows for the stiffness tuning element to be easily attached to an external structure. Finally, the silicone matrix allows for greater

adhesion than could be achieved with just the composite, since the particular silicone used (i.e. Dragon Skin 10) is softer than the composite and, therefore, allows for more conformal contact.

In order to control the temperature of the contact pad, a thermistor (10 k Ω NTC, Uxcell) was embedded between the silicone matrix and the stiffness tuning element (see Figure 2.1C). This was achieved by cutting a slit in the silicone matrix, then inserting the thermistor and sealing the slit with a flexible adhesive (Sil-Poxy, Smooth-On). The thermistor is used to measure the temperature of the stiffness tuning element, and the temperature is used as feedback for a proportional controller run by a microcontroller (Arduino Uno). The proportional controller restricts the flow of current to the flexible heater in order to maintain a desired setpoint temperature. Although the temperature at which the composite reaches its soft state is $T_{\text{soft}} \approx 67^\circ\text{C}$ (as shown in Figure 2.2), testing revealed that the thermistor reading at which this transition occurred was $\tilde{T}_{\text{soft}} \approx 48^\circ\text{C}$. So, the setpoint of the proportional controller was established at 50°C . Correspondingly, it was determined that the thermistor reading at which the composite stiffens is $\tilde{T}_{\text{stiff}} \approx 35^\circ\text{C}$.

The time scale of the transition between the stiff and soft states of the contact pad was determined by running a heating test three times. The test started with the contact pad in its stiff state at room temperature (21°C). Power was then supplied to the heater at 9.0 V, drawing approximately 1.9 A (17 W), and the contact pad was heated until it reached its setpoint temperature $\tilde{T}_{\text{set}} = 50^\circ\text{C}$. Then, power was removed from the heater, and the pad was allowed to passively cool until the thermistor reading returned to room temperature. During these tests, the average time required for the contact pad to heat from room temperature to its setpoint temperature was 3.3 minutes ($\dot{T}_{\text{heat}} = 0.15^\circ\text{C s}^{-1}$). The average time required to cool from the setpoint temperature to $\tilde{T}_{\text{stiff}} \approx 35^\circ\text{C}$ was 4.5 minutes ($\dot{T}_{\text{cool}} = 0.055^\circ\text{C s}^{-1}$).

The effectiveness of the contact pad in adhering to objects of various shapes and sizes is dependent upon its ability to conform to surfaces in its soft state. So, when designing a gripper with an integrated contact pad, the priority was to enable the contact pad to conform to objects with minimal constraints. The result was the design shown in Figure 2.1B. This gripper is a modified version of the PhantomX Parallel AX-12 Gripper (Interbotix). The parts were fabricated from VeroWhite using an Objet 3D printer. The primary modification to the original gripper design was the addition of fastening structures on the gripper jaws, which could be used to secure the contact pad to the gripper. The gripper was then mounted to a four degree of freedom (DOF) robotic arm (uArm, UFactory), as shown in Figure 2.1A.

This gripper works by modulating the distance between its jaws when the contact pad is in its soft state. At the beginning of a grasp cycle, the contact pad is in its default, flat shape. As the contact pad transitions to its soft state, it sags slightly due to gravity. Moving the gripper jaws towards each other causes the pad to buckle and deform towards the ground. The robot arm then moves the gripper downwards until the pad is brought into contact with the target object. Once sufficient contact has been established between the pad and the object, the gripper stops moving and power is removed from the flexible heater. The contact pad is then allowed to cool until it reaches its stiff state, at which point the gripper is lifted back up with the object in its grasp.

2.2.3 Experimental Setup

In order to evaluate the effectiveness of the gripper, pull-off tests [28, 43, 44] were conducted using a materials testing machine (Instron 5969). During the tests, the gripper was attached to a ± 10 N load cell that was mounted to the crosshead of the Instron, and an acrylic substrate was fixed in place directly below. Each individual test started with the contact pad in its stiff state and flat shape. The pad was then heated to $\tilde{T}_{\text{set}} = 50^\circ\text{C}$, and the gripper jaws were moved towards each other in order to cause the pad to buckle, resulting in a curved shape. In this curved shape, the contact pad is deflected downwards, with the bottom several millimeters above the surface of the acrylic substrate. Next, the Instron crosshead was lowered at 0.167 mm s^{-1} until reaching a pre-determined height. The contact pad was then allowed to rest on the substrate for 5 minutes before the Instron crosshead began retracting upwards at 0.167 mm s^{-1} . The test ended when the crosshead returned to its starting height. During the test, the Instron records force measurements from the load cell, as well as timestamps and the position of the crosshead. This testing procedure is graphically depicted in Figure 2.4A/B. Prior to each test, the contact pad and acrylic substrate were cleaned in order to ensure consistent adhesion.

Throughout pull-off testing, several parameters were chosen to be varied systematically. These parameters included the geometry and state of the contact pad, and the geometry of the acrylic substrate. The geometry of the contact pad was controlled by varying the distance between the gripper jaws and the resting height of the Instron crosshead. These parameters are represented by the variables S and H , respectively, depicted in Figure 2.4D. The state of the contact pad prior to retraction (Figure 2.4A/B, Step 5) was either state = soft or state = stiff. In the case of state = soft, the contact pad was kept at $\tilde{T}_{\text{set}} = 50^\circ\text{C}$ throughout the entire trial. In the case of state = stiff, power was removed from the flexible heater after the Instron crosshead stopped moving downwards (Figure 2.4A, Step 3). The contact pad was then allowed to cool during the 5 minute resting period, such that its temperature was below $\tilde{T}_{\text{stiff}} \approx 35^\circ\text{C}$ once the crosshead began pulling upwards. The geometry of the acrylic substrate was varied between flat and cylindrical. A minimum three tests were conducted for each unique parameter combination.

2.2.4 Finite Element Model ²

In order to gain insight into the mechanics of the gripper, a finite element model was developed to simulate its deformation and adhesion. Finite element analysis (FEA) was conducted using ABAQUS/Standard (ABAQUS 2018). The system was modeled as a two-dimensional beam under plane strain conditions and consisting of a stiffness-tunable core between two soft outer layers as shown in Figure 2.5A. The initial length of the beam is $S_0^* = 98\text{ mm}$ and the thickness of the bottom, center, and top layers are $t_1 = 0.5\text{ mm}$, $t_2 = 1.5\text{ mm}$, and $t_3 = 1\text{ mm}$, respectively. Here, S_0^* corresponds to the sum of the initial parallel jaw separation S , as shown in Figure 2.4D, and twice the distance between the location of applied clamping force and the corresponding inside parallel jaw surface. The soft outer layers were assumed to be linear elastic with Young's modulus

²Finite element model implemented by Christopher J. Stabile, Department of Mechanical Engineering and Applied Mechanics, University of Pennsylvania, Philadelphia, Pennsylvania, USA.

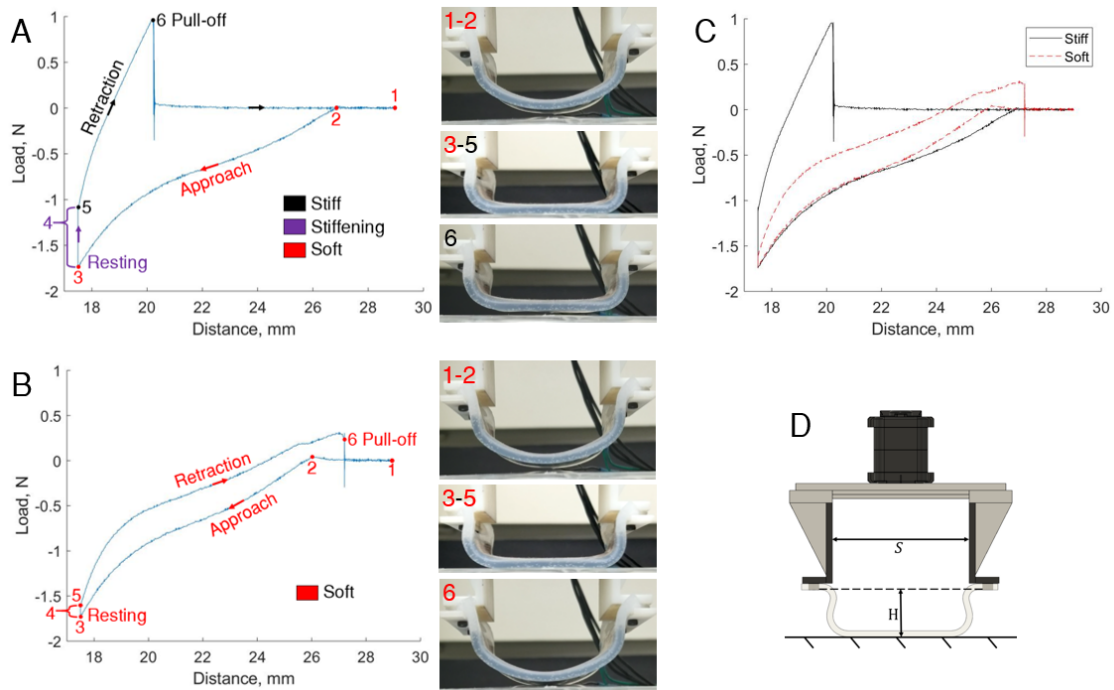


Figure 2.4: **(A)** Pull-off testing procedure for state = stiff: (1) Initially, the contact pad is in its soft state, with the bottom edge several millimeters above the acrylic substrate. Then, the Instron crosshead begins moving downwards. (2) Contact pad comes into contact with the substrate. (3) The crosshead reaches its resting height and stops moving. (4) Contact pad is allowed to rest on the substrate for 5 minutes. During this time, stress relaxation occurs due to the viscoelasticity of the composite. (5) Crosshead begins retracting. (6) The pad loses contact with the substrate. Afterwards, the crosshead continues moving upwards until it reaches its starting height. **(B)** Pull-off testing procedure for state = soft. This is identical to the stiff state procedure except for heating of the contact pad. The plots and images shown correspond to tests with parameters, $S = 46$ mm, and $H = 17.5$ mm on a flat substrate. **(C)** State = stiff and state = soft loading cycles overlaid. **(D)** Parameters controlling contact pad geometry. S is the distance between the gripper's jaws and H is the distance between the bottom of the gripper jaws and the top of the acrylic substrate.

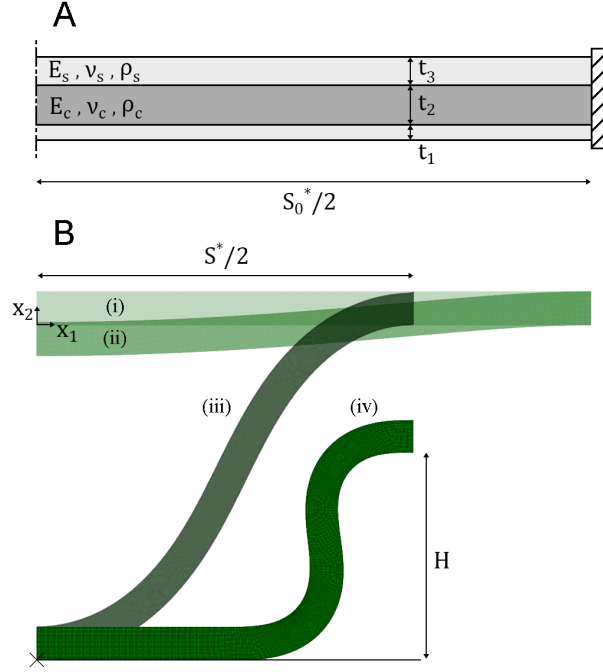


Figure 2.5: **(A)** Finite element schematic of the initial flat state. **(B)** Finite element deformation process showing (i) the initial flat state, (ii) application of gravity, (iii) compression, and (iv) contact formation.

$E_s = 0.09$ MPa, Poisson’s ratio $\nu_s = 0.49$, and density $\rho_s = 1.07$ g/cm³, representative of Dragon Skin 10. The core was assumed to be linear elastic with Young’s modulus and Poisson’s ratio defined as $E_c^{\text{soft}} = 2$ MPa and $\nu_c^{\text{soft}} = 0.49$ for the soft state and $E_c^{\text{stiff}} = 500$ MPa and $\nu_c^{\text{stiff}} = 0.45$ for the stiff state, and constant density $\rho_c = 1.145$ g/cm³. The material properties used for the core are representative of PCL, with the Young’s moduli corresponding to the soft and stiff state storage moduli of the PCL composite that was characterized through DMA as shown in Figure 2.2.

Simulations were conducted using a structured mesh consisting of plane strain eight-node hybrid biquadratic elements (CPE8H). Only half of the beam was modeled, with a symmetry condition along $x_1 = 0$ and a clamped condition along $x_1 = S_0^*/2$ as shown in Figure 2.5A, meaning that the edge nodes displace uniformly. Additionally, a surface-to-surface contact interaction with a “hard” contact pressure-overclosure relationship and frictionless behavior was specified between the beam and an analytical rigid surface. The simulations were conducted in three stages consisting of (1) deformation and contact formation, (2) soft-to-stiff transition, and (3) retraction.

During the first stage of the simulations, the beam was deformed and brought into contact with an analytical rigid surface through displacement of the clamped edge. This process involved four sub-stages including (i) initial flat state, (ii) application of gravity, (iii) compression, and (iv) contact formation. The complete deformation process is depicted in Figure 2.5B. First, the displacement components of the clamped edge were fixed and gravity was activated with a gravitational acceleration $g = 9.807$ m/s². The application of gravity was necessary to introduce an asymmetry in the beam deflection so that it would buckle in the appropriate direction. Second, the clamped edge

was displaced inward to induce buckling while establishing the desired parallel jaw separation S . Third, with an analytical rigid surface positioned into point contact with the buckled beam, the clamped edge was displaced downward to form the contact while establishing the desired clamping height H . Subsequently, the normal displacement of the nodes in contact were fixed with a displacement boundary condition, allowing for the removal of the specified contact interaction.

After achieving the deformed configuration corresponding to the desired values of S and H , the material properties of the core were changed from E_{soft} and ν_{soft} to E_{stiff} and ν_{stiff} . Meanwhile, the reference configuration of the core elements was set equal to the current/deformed configuration to effectively remove the existing strain.

For the final stage of the simulations, the clamped edge was displaced upward by some small δ and the corresponding load-displacement curve was used to determine the compliance of the system. This was done both prior to and after stiffening the core, in order to evaluate results for state = soft as well as state = stiff, respectively. For an elastic layer adhered to a rigid substrate, the normal adhesion force capacity scales with the reciprocal square root of the system compliance [47], expressed as:

$$F_c \propto \frac{1}{\sqrt{C}} \quad (2.1)$$

This allows for an estimate of the ratio of stiff to soft pull-off forces for a set of S and H values through an assessment of the change in system compliance.

2.3 Results and Discussion

2.3.1 Pull-off Testing

Results from pull-off testing are shown in Figures 2.6 and 2.7. For convenience, we consider results from tests with a flat substrate separately from those with a cylindrical substrate.

Beginning with the flat substrate results shown in Figure 2.6, it is evident that pull-off force increases when the contact pad is in its stiff state, rather than its soft state, prior to retraction. The increase in pull-off force as a result of this stiffness change was $\sim 2\text{-}6\times$, depending on gripper geometry. This finding is consistent with the results of other studies that explored stiffness modulation for tunable adhesion [28, 36].

We also see that the pull-off forces corresponding to soft state tests are approximately constant regardless of gripper geometry. This result can be explained by the fact that the deformed shape corresponding to some combination of S and H values prior to retraction is not maintained during retraction without a stiffening of the core to “lock in” the shape. Instead, as the Instron crosshead is retracted, the non-adhered regions of the contact pad straighten and the pad gradually peels from the substrate. Still, the clamping distance S will affect the peeling angle and, thus, the peel strength. However, this did not result in any significant change in pull-off force.

On the other hand, gripper geometry had a significant influence on pull-off force during stiff state tests. In the stiff state, the deformed shape prior to retraction is locked in. Furthermore, unlike in

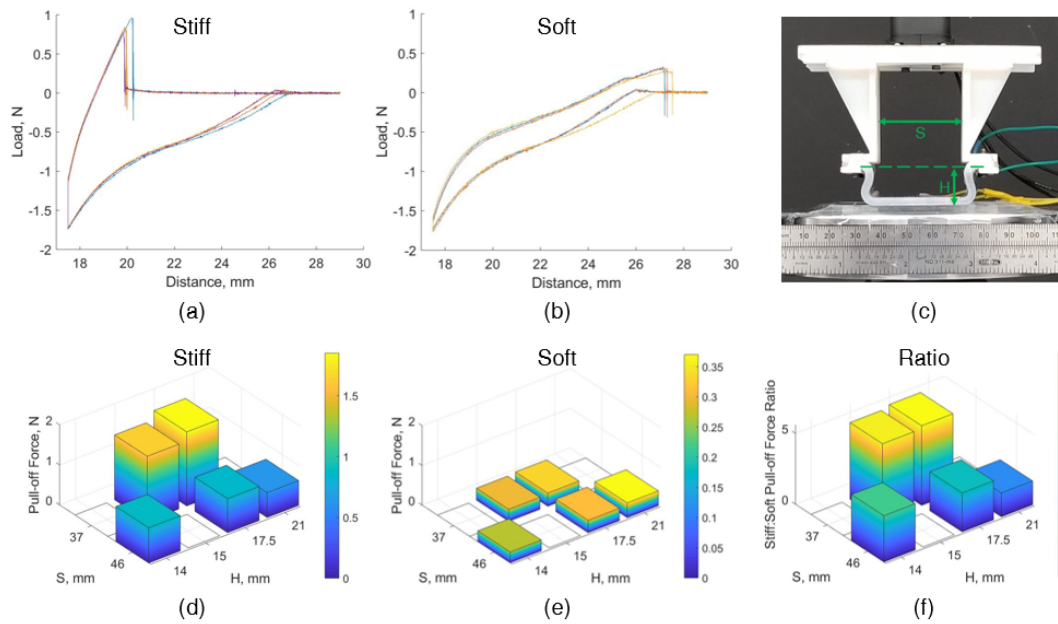


Figure 2.6: Pull-off test results for the flat substrate: **(a)** Superimposed loading cycles from consecutive trials with parameters state = stiff, $S = 46$ mm, $H = 17.5$ mm. **(b)** Superimposed loading cycles from consecutive trials with parameters state = soft, $S = 46$ mm, $H = 17.5$ mm. **(c)** Representative photograph, $S = 37$ mm, $H = 15$ mm. **(d)** Averaged results for tests with condition state = stiff. **(e)** Averaged results for tests with condition state = soft. **(f)** Ratio of pull-off force between stiff and soft conditions.

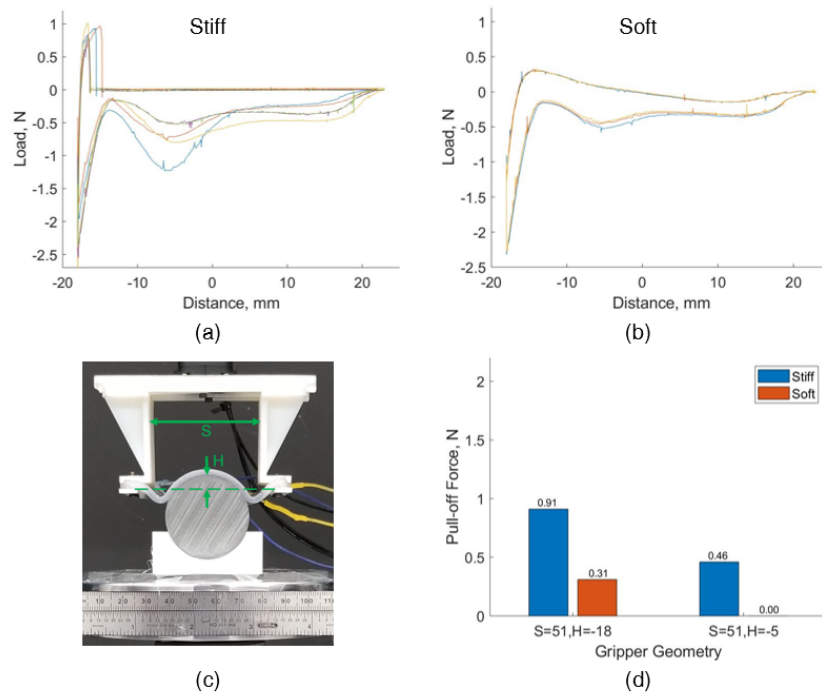


Figure 2.7: Pull-off test results for the cylindrical substrate: **(a)** Superimposed loading cycles from consecutive trials with parameters state = stiff, $S = 51$ mm, $H = -18$ mm. **(b)** Superimposed loading cycles from consecutive trials with parameters state = soft, $S = 51$ mm, $H = -18$ mm. **(c)** Representative photograph, $S = 51$ mm, $H = -5$ mm. **(d)** Averaged results, S held constant at 51 mm.

the soft state, the contact area between the gripper and the substrate just prior to pull-off is virtually the same as the original contact area. Without peeling, the pull-off force is governed by the normal adhesion strength, which is influenced by load sharing on the interface. In general, stiffer materials allow for improved load sharing and, thus, adhesion enhancement. Similarly, the gripper geometry can affect the stress distribution on the interface, which can result in changes in pull-off force. The results show that as S is held constant and H increases, pull-off force tends to decrease, and that as H is held constant and S increases, pull-off force tends to decrease. However, these results are based on a limited amount of data, and more testing will be required in order to arrive at a definitive conclusion regarding the impact of gripper geometry on pull-off force.

When analyzing results from tests with the cylindrical substrate in Figure 2.7, it is evident that the trend of increased pull-off force for stiff versus soft state tests still holds. As with the flat substrate, we see that as S is held constant and H increases, the pull-off force decreases. The magnitudes of the pull-off force are also similar to what was observed with the flat substrate.

One possible source of uncertainty from the pull-off testing is that the contact pad was prone to experiencing small amounts of plastic deformation during testing. We believe this was due to the fact that the flexible heater did not cover the entire area of the composite's surface (see Figure 2.3a). Consequently, the edges of the composite (not covered by the heater) were not always raised to the same temperature as the rest of the composite, which prevented them from fully softening and caused them to retain a small amount of curvature as the contact pad was continuously stretched (flattened) and compressed (curved) over the course of many loading cycles.

2.3.2 Comparison of FEA and Experimental Results

Using the finite element model described in Section 2.2.4, the gripper's deformed profile after contact formation was examined for several combinations of S and H . Generally, the predicted profiles show good agreement with the experimental profiles, as exemplified by the profiles shown in Figure 2.8.

To estimate the ratio of stiff to soft pull-off forces, the system compliance was determined for sets of S and H values in both the stiff and soft states. For all combinations of S and H considered, use of Eq. 2.1 yielded a stiff to soft pull-off force ratio of ~ 12 . From a compliance perspective, and considering the $250\times$ increase in the Young's modulus of the core material upon stiffening, the stiff to soft pull-off force ratio is expected to be in the range of $\sim \sqrt{250}$. This suggests a $16\times$ increase in pull-off force, which is comparable to the $12\times$ increase predicted by FEA. These ratios are larger than those given by the experimental data, which shows up to a $6\times$ increase in pull-off force from stiffening the core. The difference between the FEA prediction and the experimental results could be attributed, in part, to misalignment between the gripper and substrate in the experiments that would reduce the measured pull-off force.

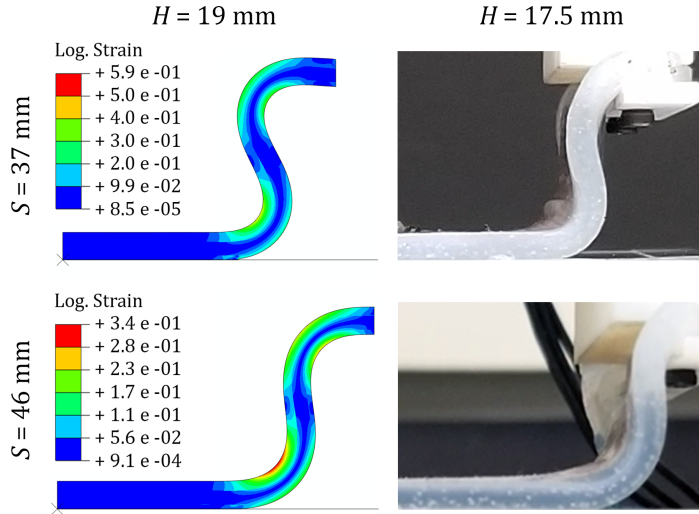


Figure 2.8: Deformed profiles of the contact pad prior to retraction. Predictions from FEA with logarithmic maximum principal strain contours are shown in the left column, and experimental results are shown in the right column.

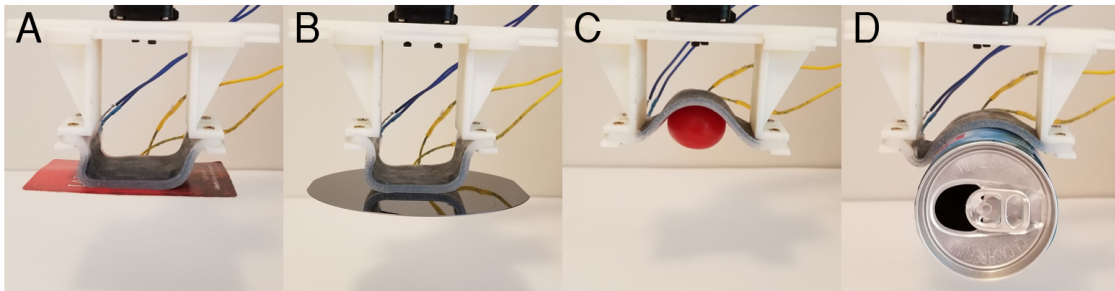


Figure 2.9: Grasping various objects: (A) Playing card, 1.62 g. (B) Silicon wafer, 9.38 g. (C) Small tomato, 25.3 g. (D) Juice can, 36.6 g.

2.3.3 Pick-and-place Demonstrations

In addition to pull-off testing, the gripper’s efficacy was also evaluated based on pick-and-place demonstrations conducted with various objects. Objects successfully grasped and released included a playing card (1.62 g), a silicon wafer (9.38 g), a small tomato (25.3 g), and a juice can (36.6 g), shown in Figure 2.9.

In general, we found that this gripper excels at grasping flat, smooth objects, which can be challenging for grippers that grasp objects via force closure. It was even capable of lifting a small dinner plate weighing 147 g (1.44 N), corresponding to 78% of the maximum pull-off force measured during pull-off testing. The gripper is also capable of grasping objects with convex surfaces of various shapes and sizes, including a tomato and a juice can, as shown in Figure 2.9. Although this capability is generally limited to objects with simple, rounded surfaces, it serves to demonstrate the gripper’s versatility. The gripper also showed promise in handling fragile objects - such as the silicon wafer and the tomato - without causing any damage to them. This capability is a

result of the gripper’s inherent compliance, and does not require any special control strategies. After grasping, each of the objects was released and returned to near its original location by simply heating the contact pad and allowing the object to drop due to the decreased adhesion force.

Taken as a whole, these pick-and-place demonstrations are a validation of the gripper’s applicability towards real-world tasks. Although there are several classes of objects which the gripper cannot reliably grasp - including those with rough or wet surfaces (which are problematic for many grippers that rely upon dry adhesion) or complex surface geometries - it exhibits an impressive degree of versatility given its simplicity. Importantly, because of the gripper’s simplicity - specifically the fact that it requires only a single servo motor for actuation and a 9V power supply to power the flexible heater - it can be easily integrated with most robotic systems, including the small uArm robot that was used for these demonstrations.

2.3.4 Limitations

While the gripper developed for this study has demonstrated its ability to successfully grasp and release various objects, it does have some limitations. First is the gripper’s cycle time. Since the gripper’s stiffness tuning capability is dependent on a thermally-induced phase change, the amount of time required to perform a successful grasp is relatively large. Quantitatively, the gripper requires on average 3.3 minutes to heat from room temperature to $\tilde{T}_{\text{set}} = 50\text{ }^{\circ}\text{C}$ and 4.5 minutes to cool to $\tilde{T}_{\text{stiff}} = 35\text{ }^{\circ}\text{C}$ (as established in Section 2.2.1), resulting in an overall cycle time of 8.8 minutes to grasp a single object. This issue is common among stiffness tuning technologies that rely upon thermal activation. However, there are several steps that could be taken in future work to reduce this cycle time. One solution is to load the contact pad’s silicone matrix with liquid metal in order to increase its thermal conductivity, as established in [48]. Another solution is to implement active cooling by running cold fluid through the contact pad while it cools, as demonstrated in [27, 30, 49]. Additionally, the PCL composite could be replaced with a material with a lower melting point and higher thermal conductivity.

Another limitation of the current gripper is that it is not always successful in releasing objects after grasping. In principle, when the gripper is ready to release an object, the contact pad can be heated to $\tilde{T}_{\text{set}} = 50\text{ }^{\circ}\text{C}$ and the gripper jaws can be separated, which should result in a decrease in adhesion strength and subsequent release of the object. However, while this strategy is typically successful, there are instances in which the decrease in adhesion strength is not sufficient to enable release. This is especially true for lightweight objects, such as a playing card. One possible solution to this problem would be to replace the PCL composite with a shape memory polymer, which could be “programmed” to alter its surface geometry during release, as demonstrated in [21].

Finally, the gripper’s maximum payload capacity - approximately 1.85 N, as measured during pull-off testing - is also a potential limitation. The payload capacity of the gripper is governed by a number of factors, including the circumferential length (perimeter) of the contact interface [43] and the stress distribution at the interface. In order to increase the perimeter of the contact interface, the size of the contact pad would need to be increased, which is not a preferred solution. On the other hand, some studies have shown that the stress distribution at the interface can be controlled

using kirigami-based structures [50], enabling increased adhesion strength. This kirigami-based approach may be a promising avenue for further investigation.

2.4 Concluding Remarks

This research focused on the development of a novel soft robotic gripper that relies upon stiffness and adhesion tuning capabilities enabled by controlling the temperature of a thermoplastic composite embedded in a soft contact pad. Pull-off tests performed using the gripper showed that stiffness tuning leads to enhanced adhesion, and provided insight into the effect of gripper geometry and substrate geometry on adhesion strength. A finite element model was also developed to simulate the testing procedure, which provided insight into the deformation and adhesion mechanics of the system. Finally, the gripper was integrated with a 4 DOF robotic arm, and used to successfully grasp and release objects of various shapes, weights, and sizes.

Chapter 3

Design Optimization of a Tendon Driven Foam Hand

3.1 Background

For several decades, roboticists have endeavoured to develop autonomous systems capable of dexterous manipulation [6, 8]. Although substantial progress has been made towards the ultimate goal of achieving human-level dexterity, this still remains an extremely challenging and unsolved problem. Recently, however, progress in reinforcement learning (RL) for robotics has enabled unprecedented levels of dexterity from autonomous robot end effectors, culminating in the ability of an anthropomorphic hand to reorient a cube to any desired configuration [51]. This result represents the current state of the art in autonomous robotic manipulation. However, such a result may not be easily reproducible, owing to the prodigious amount of effort and resources required.

The difficulty in producing this cutting-edge result [51] can largely be attributed to the hardware being used - the Shadow Dexterous Hand (Shadow Robot Company) - a 24 degree of freedom (DoF), 20 degree of actuation (DoA) robot hand, costing on the order of tens of thousands of US dollars. Control of such a complex, high dimensional system is a dauntingly difficult task, and research is made yet more difficult by the fact that the system is prone to experiencing frequent breakages throughout testing [51]. Unfortunately, there few alternative hardware options, since the Shadow Hand is one of the only commercially available robotic hands which possesses sufficient dexterous capabilities to accomplish a variety of complex manipulation tasks. Clearly, in order for other research centers and universities with limited resources to get involved in research on dexterous manipulation - and in doing so help to advance the state of the art - a low cost, low complexity dexterous manipulation platform will be critically important.

In fact, several groups have developed dexterous manipulation platforms intended (at least in part) to address this problem, many of which rely upon the principles of soft robotics [6, 9] in order to achieve high dexterity while minimizing cost and complexity. Soft robotic manipulators are well-suited for this problem for several reasons. First, they can be fabricated using rapid prototyping

techniques, such as 3D printing and laser cutting, and low cost materials, such as plastics and rubbers, which reduces the overall cost of the robot. Second, soft robots are typically more robust than rigid robots, since their deformable structures allow them to absorb impacts without being damaged. Finally, soft robots are able to conform and adapt to their environments due to their compliance, which reduces the need for precision in control.

Examples of dexterous soft robotic end effectors include the RBO Hand 2 [4], a silicone-based, pneumatically actuated anthropomorphic hand with 7 DoAs; the Pisa/IIT SoftHand 2 [52], a compliant, tendon-driven anthropomorphic hand with 2 DoAs, relying upon “adaptive synergies” [53] for simplified actuation of many joints; and several tendon-driven hands with flexure joints [54–56], developed as a part of the Yale OpenHand Project, all of which have less than 5 fingers and between 2 and 4 DoAs. However, it is the author’s opinion that none of these end effectors have demonstrated an ability to accomplish a sufficiently *wide range* of dexterous in-hand manipulation tasks. Another notable soft robotic manipulator is the highly biomimetic, compliant, tendon driven hand developed by Xu and Todorov [57]. This hand demonstrates high levels of dexterity, but is still rather complex, with many intricate parts susceptible to breakage, as well as a relatively high actuation dimensionality (10 DoAs).

The goal of this work is to bridge the gap between dexterity and complexity by developing a robotic end effector which demonstrates a high level of dexterity while requiring a low number of actuators, i.e. control inputs, in order to operate. This work will build upon the work of King et. al [13, 58, 59], who developed techniques for fabricating and controlling tendon-driven hands made almost entirely of foam. Various prototypes developed using this foam-based architecture have demonstrated promising levels of dexterity. Importantly, the *potential* dexterity of these foam hands is nearly unlimited, since fabrication techniques allow for the establishment of any desired morphology, which can be actuated with a theoretically unlimited number of tendons in any desired configuration. Of course, there are practical limitations on the number of motors that can be used to drive these tendons, and the dexterous hands developed in [13, 58, 59] used 10 motors to drive an equal number of tendons. The contribution of this work will be to optimize the design of these hands such that the number of required motors can be reduced while maintaining a high level of dexterity.

Reducing the number of motors used by the hand is important for several reasons. First, this reduces the actuation dimensionality of the system, which enables simplified control. Second, less motors means a less expensive system. Finally, a reduction in motors leads to a reduction in the overall weight and bulk of the hand, which is important for integration with robotic arms. In order to assess how many motors are acceptable based on these criteria, we can draw comparisons with the hands developed for the Yale OpenHand Project [54–56], which were designed specifically to meet the needs of researchers as outlined above, i.e. simplicity, low cost, and ease of integration with common robotic arms such as the Barrett WAM arm and Rethink Robotics’ Baxter. Since the most complex hands developed for the OpenHand Project are actuated by 4 servo motors, this will serve as our benchmark for the maximum number of allowable motors.

The rest of this chapter is structured as follows: in Section 3.2, we first establish a new bench-

mark for evaluating the dexterity of robot end effectors. We then describe the specific morphology and tendon routing chosen for our optimized hand design, and introduce the concept of postural synergies [60], which can be exploited to reduce actuation dimensionality without significant losses in dexterity. In Section 3.3, we evaluate the hand’s performance using the previously established dexterity benchmark test, comparing results from the fully actuated case to results from the underactuated case (exploiting synergies), and discuss limitations of the study. Finally, we offer concluding remarks in Section 3.4.

3.2 Methodology

3.2.1 Evaluating Dexterity

Throughout the rest of this chapter, we will define dexterity as “the capability of changing the position and orientation of the manipulated object from a given reference configuration to a different one, arbitrarily chosen within the hand workspace” [8]. Specifically, we are interested in *in-hand manipulation* (a term used interchangeably with dexterous manipulation throughout this chapter), which involves controlling the pose of a grasped object using *only* the hand, without relying on the arm or body. It is also important to make a distinction between *dexterous manipulation* and *grasping*. Grasping has been extensively studied and characterized by the robotics community, and involves “an action of a hand on an object consisting in preventing its motions relative to the hand, possibly in the face of disturbance forces acting on the object itself” [8]. In other words, grasping is a fundamentally static operation, whereas dexterous manipulation is a fundamentally dynamic operation. Many robotic end effectors have been developed with the goal of achieving robust grasps for a wide range of objects, but because the objectives of grasping and dexterous manipulation are at odds, the design requirements for these end effectors may vary widely from the design requirements for hands intended for dexterous manipulation.

We can also define the *range of dexterity* of a hand using a classification proposed by Bullock et. al [61], which categorizes in-hand manipulation tasks based on rotations and translations along hand coordinate axes. They further categorize in-hand manipulations according to whether or not there is motion at contact - in other words, whether the initial contact points made between the hand and object remain fixed throughout a given manipulation. In total, this classification establishes 12 distinct categories of in-hand manipulation, corresponding to individual rotations and translations along each axis in 3D space (e.g. θ_x , Δ_x , θ_y ...), for cases of either motion at contact (A) or no motion at contact (NA). It should be noted that the authors could not find a human manipulation pattern corresponding to θ_y (A), reducing the size of the set of possible in-hand manipulation categories to 11. Thus, the range of dexterity of a given robotic end effector can be evaluated based on how many of the 11 possible in-hand manipulation categories established in [61] are feasible.

Ideally, there would be one or more quantitative metrics which could be used to evaluate an end effector’s ability to accomplish tasks corresponding to each of these 11 manipulation categories. These metrics could then be used as parameters in an optimization which would produce a hand

with maximal dexterity. One prominent example of a quantitative metric for dexterity evaluation is calculating the area of an end effector’s “reachable configuration manifold” [56]. However, this metric is limited to translations in two dimensions, during which there is no motion at contact, and thus only covers a small subset of all possible in-hand manipulations. As of this writing, no corresponding metrics have been established which can be used to evaluate the remaining categories of in-hand manipulation. Thus, we must forgo quantitative metrics for dexterity evaluation in favor of qualitative tests.

Somewhat surprisingly, no qualitative benchmark tests have yet been established within the robotics literature which can be used to sufficiently evaluate an end effector’s dexterity. One test which some authors have used to measure dexterity is the Kapandji test [62], which evaluates the ability of the thumb’s distal phalanx to contact different locations around the hand. However, this test can only be used to evaluate anthropomorphic hands, and is at best a rough proxy for measuring a hand’s dexterous capabilities. There are also various hand function tests used within the fields of physical rehabilitation and prosthetics, such as the Jebsen Taylor Hand Function test [63], the Purdue Pegboard test [64], and the Box and Blocks test [65], but these tests are generally limited to pick-and-place tasks and simple tool usage, which primarily measure grasping ability and whole-arm dexterity, as opposed to in-hand manipulation capability. Thus, there is a need for a new benchmark test which can be used to evaluate the full range of dexterous in-hand manipulation capabilities of a hand.

We propose a benchmark test based on a manipulation classification established by Elliott and Connolly [66]. This classification consists of 13 distinct in-hand manipulation patterns, derived from observations of multiple human subjects. We find that this classification is well-suited for adaptation as a dexterity benchmark test for several reasons. First, and most importantly, across the 13 manipulation patterns established in [66], each of the in-hand manipulation categories from [61] is represented at least once. Thus, we can claim that any end effector capable of performing all of these patterns is accordingly capable of performing the full range of possible in-hand manipulations. Second, across these 13 patterns, all of the primary sub-classes of in-hand manipulation, namely finger-gaiting, rolling, and sliding [8], are represented. Finally, this classification includes detailed descriptions and illustrations of each manipulation pattern, which greatly enhances its clarity and interpretability.

In order to establish a benchmark test based on these manipulation patterns, it is necessary to define criteria which dictate whether an attempted pattern has been “passed” or “failed”. These criteria are based on the descriptions and illustrations from [66], and can be found in Appendix A. As a further measure for enabling objective evaluation of these patterns, videos have been recorded of a human hand performing each pattern according to the established criteria, which can be compared to videos of a robot hand performing the same patterns. Ultimately, it is up to the subjective judgement of each observer to determine whether each pattern has been performed successfully, but we have done our best to establish a standard method for evaluation.

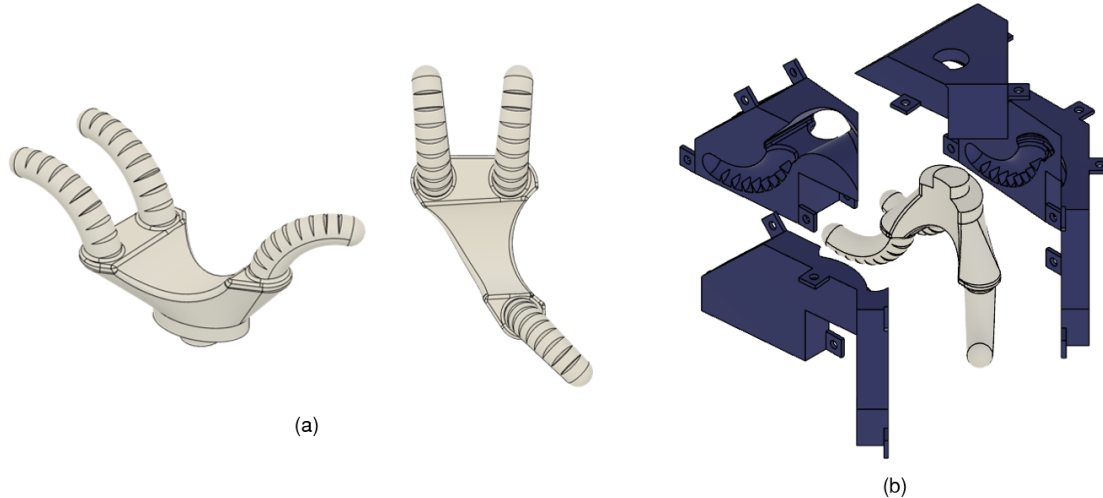


Figure 3.1: (a) CAD images of the foam hand prototype. (b) CAD model of the multi-part mold used to fabricate the foam hand.

3.2.2 Morphology

The first step in establishing a suitable morphology for this foam hand prototype was to limit the number of fingers to three. This is the theoretical minimum number of fingers required to perform each of the 13 manipulation patterns from [66], as can be demonstrated by a human subject. Limiting the number of fingers reduces the number of tendons needed for actuation, which in turn reduces the number of motors required to drive the tendons.

Next, a three-fingered, bio-inspired morphology was established, based on the thumb, index, and middle fingers of a human hand in both shape and dimensions, as shown in Figure 3.1a (a dimensioned drawing can be found in Appendix D). Figure 3.2 shows a comparison between coordinate axes of the foam hand prototype and a human hand. The foam hand is fabricated as a single, continuous piece of foam by creating a multi-part mold using a 3D printer, shown in Figure 3.1b. Because the flexibility of foam-based hands enables an exceptional range of motion, this bio-inspired design is able to closely imitate many of the postures formed by human hands during in-hand manipulation. This simplifies manual control of the robot, since the necessary postures for any manipulation pattern can simply be copied from a human example.

Importantly, each of the fingers of the foam hand is initially curled away from the palm when the hand is in its rest pose, i.e. when no external forces are acting on the hand. The purpose of this design choice is to eliminate the need for extensor tendons running along the backsides of each finger. With this design, the hand relies upon the elasticity of the foam for the extension of each finger. In order to avoid buckling due to excessive deformation during flexion, slits are introduced along the fronts of each finger.

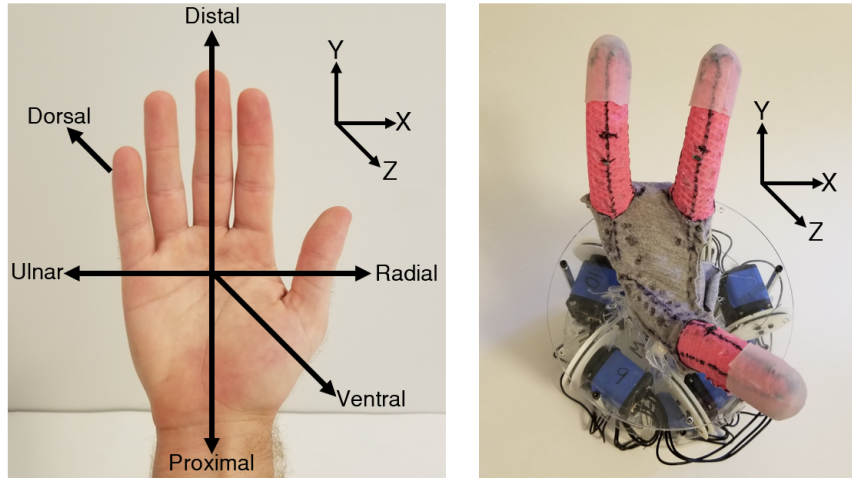


Figure 3.2: Coordinate axes for a human hand (left) and the foam hand prototype (right).

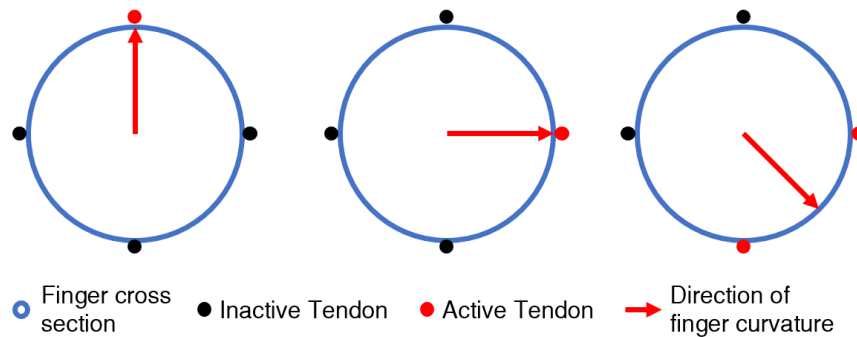


Figure 3.3: Diagram illustrating how a foam finger can be actuated with four tendons in a way that allows it to bend in any direction.

3.2.3 Tendon Routing

In order for this foam hand prototype to achieve maximal dexterity, it is advantageous for its fingers to be able to bend in any direction. This can be achieved by running four equally spaced tendons along the length of each finger, as shown in Figure 3.3. For the specific morphology established in Section 3.2.2, only three tendons are required in order to achieve this functionality, due to the intrinsic curvature of each finger.

Two important modifications were made to this basic tendon routing scheme based on the results of early testing with the hand. First, it was determined that the tendons running along the outsides of the index and middle fingers (the radial tendon on the index finger and the ulnar tendon on the middle finger) were generally not needed for any of the 13 manipulation patterns from [66], and thus could be eliminated without any significant loss in dexterity.

Additionally, testing revealed that the positions of the hand's fingertips could not be sufficiently controlled with this default tendon routing scheme. This result can be explained through analysis

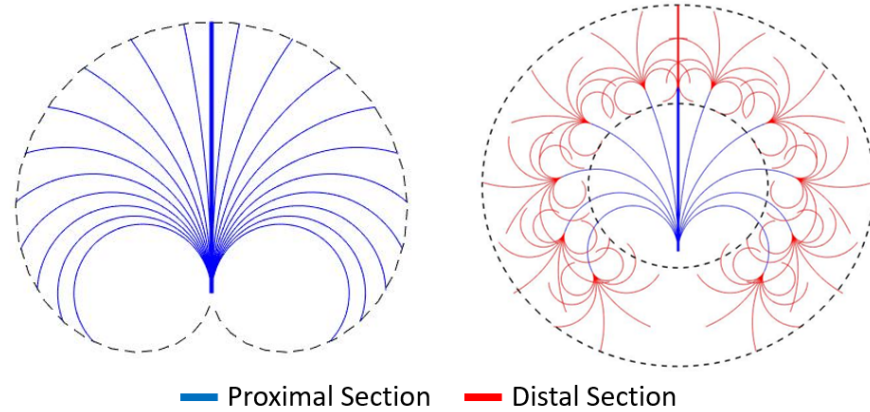


Figure 3.4: Diagram illustrating fingertip workspaces. The workspace is the area *between* dotted lines. (left) Finger actuated by individual tendons running along its length. (right) Finger actuated by multiple tendons (proximal and distal) running along its length.

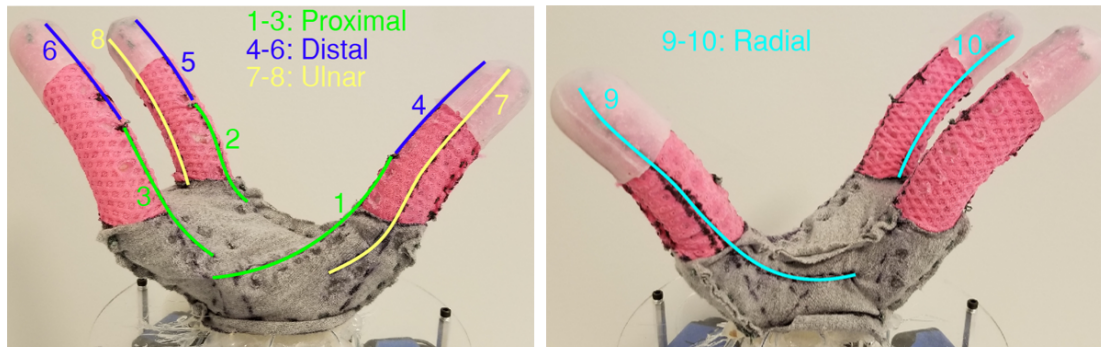


Figure 3.5: Tendon routing diagram for the final foam hand prototype.

of Figure 3.4. With only one tendon running along the length of each finger (in each direction), the workspace of the fingertips is constrained to a one-dimensional arc. Thus a second tendon must be added along the length of each finger, such that one tendon controls the finger’s proximal section, and the other tendon controls the finger’s distal section. In this manner, a multi-jointed behavior is established, which enables a fingertip workspace with a non-zero volume.

After accounting for both of these insights, the resulting hand prototype was actuated by 10 tendons - three for the middle and index fingers, and four for the thumb. A tendon routing diagram is shown in Figure 3.5. This is the the final prototype which was used for the experiments discussed in Section 3.3. For more details on the fabrication process, including the application of the fabric “glove” through which the tendons are routed and the design of the motor bank which drives the tendons, see [13].

3.2.4 Postural Synergies

Because the prototype described in the preceding sections is actuated by 10 tendons, it requires 10 motors for full actuation. In order to reduce the number of motors to less than 5, as dictated in Section 3.1, it is necessary to drive multiple tendons with individual motors. In principle, this can be achieved with limited loss in dexterous capability through the application of postural synergies [60].

Postural synergies can be thought of as manipulation primitives which consist - in the case of human hands - of the coordinated movement of multiple joints in order to achieve a specific set of postures. In humans, postural synergies arise both from physical coupling of tendons and muscles and from neuro-muscular patterns [60, 67]. Synergies can be empirically “discovered” by analyzing data from human subjects using principal component analysis (PCA), as demonstrated in a seminal paper by Santello et al. [60]. The findings of [60] were that the first two principal components, i.e. synergies, resulting from this analysis accounted for more than 80% of the total variation across all data, which led the authors to believe that this dimensionality reduction could be applied without a significant loss in functionality.

Since the work Santello et. al [60], postural synergies have been applied with some success to numerous robotic hands, including but not limited to [52, 53, 67–70]. However, in most of these cases, the goal was to enable robust grasping ability, rather than dexterous manipulation. An exception is the Pisa/IIT SoftHand 2 [52], which employs multiple “adaptive” synergies [53] for dexterous manipulation. However, the dataset from which these synergies are derived comes from [60], which consists entirely of data from *grasping* tasks, rather than dexterous manipulation tasks. As a result, the dexterous capabilities of this hand are questionable.

We propose to derive synergies from data collected by performing the 13 manipulation patterns from [66]. These patterns are performed by guiding the fully actuated foam hand prototype through manually programmed keyframes. The keyframes correspond to 10-dimensional hand posture vectors (Equation 3.1), which consist of linear displacement values for each of the hand’s 10 tendons. Each of the manipulation patterns required between 3 and 5 keyframes for completion (including an initial keyframe for each pattern corresponding to the hand’s rest pose). The input data matrix (Equation 3.2) for the principal component analysis consists of 45 total keyframes, or data points. It should be noted that only 33 of these data points are distinct, since the rest pose is repeated 13 times throughout the dataset.

$$P_i = [d_1 \quad \cdots \quad d_j \quad \cdots \quad d_M]^T \quad (3.1)$$

$$D = \begin{bmatrix} P_1^T \\ \vdots \\ P_i^T \\ \vdots \\ P_N^T \end{bmatrix} \quad (3.2)$$

The procedure for PCA is described briefly here; for a more thorough description, see [71]. First, the input data is centered by subtracting the data's centroid (Equation 3.3), which corresponds to the average displacement values for each of the hand's tendons across all input data. Next, the covariance matrix (Equation 3.5) of the centered data is calculated. The eigenvectors (Equation 3.6) of the covariance matrix represent the principal components (PCs) of the data, and the corresponding eigenvalues represent the percentage of the overall variance of the data explained by each principal component. The principal components are then ordered according to the size of their eigenvalues. Principal component vectors are analogous to vector bases - they are all linearly independent of and orthogonal to each other, and can be combined in order to span multi-dimensional spaces. As a result, we can state that if the first PC accounts for P_1 percentage of the variance in the data, and the second PC accounts for P_2 percentage of the variance, then the combination of the first two PCs accounts for $P_1 + P_2$ percentage of the variance, and so on.

$$C = [\bar{d}_1 \quad \cdots \quad \bar{d}_j \quad \cdots \quad \bar{d}_M] \quad (3.3)$$

$$D_c = D - C \quad (3.4)$$

$$S = \frac{D_c^T D_c}{N - 1} \quad (3.5)$$

$$E_j = [e_1 \quad \cdots \quad e_j \quad \cdots \quad e_M]^T \quad (3.6)$$

The centered data (Equation 3.4) can then be projected onto the principal component vectors (Equation 3.7) and reconstructed in principal component coordinate space (Equation 3.8) in order to yield low-dimensional approximations. The original data can be fully reconstructed by combining the low-dimensional reconstructions corresponding to every principal component (Equation 3.9). We follow this procedure in order to reconstruct keyframes from the original dataset using various combinations of PCs. The reconstructed keyframes are then used to perform each manipulation pattern with the fully actuated hand. This is a software-based implementation of synergies (as in [70]), since the number of control inputs is reduced while the number of actuators remains the same. The results from this software testing can then be used to guide the mechanical implementation of synergies, where each principal component is controlled using a single motor.

$$Z_j = D_c E_j \quad (3.7)$$

$$D_R^j = \begin{bmatrix} E_j^T \\ \vdots \\ E_j^T \\ \vdots \\ E_j^T \end{bmatrix} \circ Z_j + C \quad (3.8)$$

$$D = D_R^1 + \dots D_R^j + \dots D_R^M \quad (3.9)$$

Mechanical Implementation of Postural Synergies

In the literature, there are two primary methods for the mechanical implementation of synergies in tendon-driven hands. The first method is to use differential pulley mechanisms [72–74] in order to transmit the output of a single motor to multiple tendons. Differential pulley mechanisms have two primary benefits. First, their implementation is relatively simple and straightforward. Second, they allow for *adaptive* grasping. In adaptive grasping, when the movement of one finger is halted by contact with an obstruction, i.e. the object being grasped, the other finger or fingers which are coupled to the obstructed finger are able to continue moving, allowing the hand posture to adapt to the shape of the object. Differential pulley mechanisms have been used in several robotic hands to implement “adaptive synergies” in a principled fashion [52, 53].

The other method for mechanical implementation of synergies in tendon-driven hands is to use “pulley trains” [67–69], which consist of motor-driven axles with multiple pulleys fixed along their length. In this implementation, one pulley train is used to represent each synergy/principal component. For an individual pulley train, the diameters of its pulleys are proportional to the magnitudes of each element in the corresponding PC vector. For vector elements with negative magnitudes, the tendons must be wrapped around the pulleys in the opposite direction. To enable the principal components to be combined with each other, the outputs from each pulley train must be coupled. For a more detailed description of the mechanical implementation of synergies via pulley trains, see [67].

The implementation of pulley trains is much less straightforward than differential pulley mechanisms, and has several other distinct drawbacks. The first drawback is that pulley trains do not inherently enable adaptive grasping. In order to enable adaptive grasping, compliant elements, such as springs, must be introduced into the transmission path [68]. The second drawback is that there is no established method for implementing more than two PCs using pulley trains. Despite these drawbacks, we choose to implement synergies using pulley trains rather than differential pulley mechanisms because differential pulley mechanisms have limited representation power. Specifically, in differential pulley mechanisms coupled tendons must always move in the same direction (either all shortening or all lengthening). This is a critical flaw, since it greatly limits the ability of a hand to perform a wide range of dexterous manipulations.

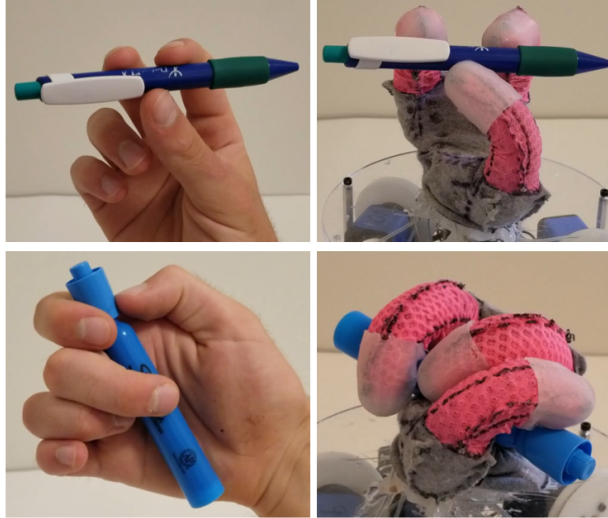


Figure 3.6: Comparisons between human and robot postures: RockII (top) and Palmar Slide (bottom).

3.3 Results and Discussion

3.3.1 Fully Actuated Hand

The fully actuated foam hand prototype described in Section 3.2 was able to successfully complete 8 of the 13 manipulation patterns from [66], based on the criteria established in Appendix A. The successfully completed manipulation patterns included Pinch, Dynamic Tripod, Twiddle, Rock, Rock II, Radial Roll, Index Roll, and Linear Step. Photo sequences of each manipulation pattern are shown in Appendix B.

With regard to the manipulation patterns which the hand was unable to perform - Squeeze, Full Roll, Rotary Step, Interdigital Step, and Palmar Slide - there were several factors which contributed towards these failures. The first of these limiting factors was the control strategy used, i.e. manually programmed keyframes. While this control strategy is straightforward to implement, it is limited by the intuition of the programmer, and has no theoretical groundings which drive it towards success. Especially for more complicated, multi-step manipulation patterns such as Rotary Step and Digital Step, it is possible that a more sophisticated control strategy, e.g. one derived via reinforcement learning, could produce successful results where manually programmed keyframes failed.

Another limiting factor was the morphology and tendon routing of the hand. While the prototype used was generally able to closely imitate the postures of a human hand for each manipulation pattern, there were some instances in which the hand failed to imitate its human counterpart due to constraints in its morphology. This was especially evident with the Palmar Slide pattern, as is shown in Figure 3.6. Additionally, it is possible that an additional finger or additional tendons, i.e. the tendons running along the outsides of the index and middle fingers which were removed after preliminary testing, may have helped the hand to accomplish some of the more complicated patterns such as Rotary Step or Digital Step.

The final limiting factor was the low stiffness and correspondingly poor force transmission capability of the hand. This is one of the primary drawbacks of a hand made entirely from soft materials, and was the main factor in the hand's inability to complete the Squeeze pattern. The task associated with this pattern involved compressing the plunger of a syringe. When attempting this task, the foam hand's fingers would consistently buckle before they could apply enough force to displace the plunger.

3.3.2 Software Synergies

Results from testing using software synergies varied depending on the amount of data used as input for the principal component analysis. Two cases were considered: one in which all of the data collected using the fully actuated hand was used, and another where only data from the successfully completed manipulation patterns was used. The results are summarized in Tables 3.1 and 3.2. These results indicate that the hand was able to complete more patterns using less principal components when only the subset of data corresponding to successfully completed manipulations was used to produce software synergies. This result is not surprising, as we would expect the PCA to yield a better fit to the successful manipulations when only the successful manipulations are used as input. There is a trade-off to consider here: when only a subset of the data is considered, the hand's ability to perform manipulations from this subset is high, but the range of manipulations which the hand can *potentially* perform is limited. In other words, we risk overfitting to the subset of successful manipulations. However, in our case the most important consideration was how many manipulation patterns could reliably be performed by the hand using only two PCs, since that is the apparent limit on the number of PCs which can be mechanically implemented using pulley trains. Accordingly, we limit the rest of our discussion to the software synergies which were produced by only considering the successful subset of manipulation patterns.

A scree plot resulting from the principal component analysis is shown in Figure 3.7. According to this plot, nearly 90% of the variance in the data is accounted for by the first two principal components. However, it should be noted that 6 principal components - accounting for 98.2% of the total variance in the data - are required in order to sufficiently reconstruct all of the successful manipulation patterns. To some extent, this result calls into question the usefulness of PCA as a dimensionality reduction method for this particular application (dexterous manipulation), since we would hope that all of the data could be sufficiently approximated with considerably less than 98% of the variance in the data accounted for.

A plot of the data reconstructed in PC coordinate space using just the first two PCs is shown in Figure 3.8a. It is readily apparent from this plot that the data can be grouped into two clusters. The cluster in the lower right quadrant of the plot corresponds to manipulation patterns which rely only on the thumb and index finger, whereas the cluster in the upper right quadrant corresponds to manipulations which require all three fingers. Although we do not take advantage of this clustering here, one potentially useful strategy could be to reduce the dataset to only a single cluster, thus obtaining a better fit for that particular cluster. Of course, this strategy comes with the disadvantage of no longer being able to perform the manipulation patterns from the excluded cluster. In some sense, this is what we are doing by omitting the failed manipulation patterns from our dataset (see

Table 3.1: Number of principal components required to complete each manipulation pattern. The “Subset” column applies to principal components which were derived using only data from manipulations which were successfully completed by the fully actuated hand. The “All Column” refers to principal components which were derived using the full dataset.

	# of PCs	
	Subset	All
Pinch	2	4
Tripod	2	5
Squeeze	-	-
Twiddle	6	4
Rock	4	5
RockII	2	4
Radial Roll	2	4
Index Roll	2	4
Full Roll	-	-
Rotary Step	-	-
Interdigital Step	-	-
Linear Step	3	4
Palmar Slide	-	-
Average	2.88	4.25

Table 3.2: Number manipulations successfully completed versus number of principal components applied. The “Subset” column applies to principal components which were derived using only data from manipulations which were successfully completed by the fully actuated hand. The “All Column” refers to principal components which were derived using the full dataset.

# of PCs	Successful Manipulations	
	Subset	All
1	0	0
2	5	0
3	6	0
4	7	6
5	7	8
6	8	8

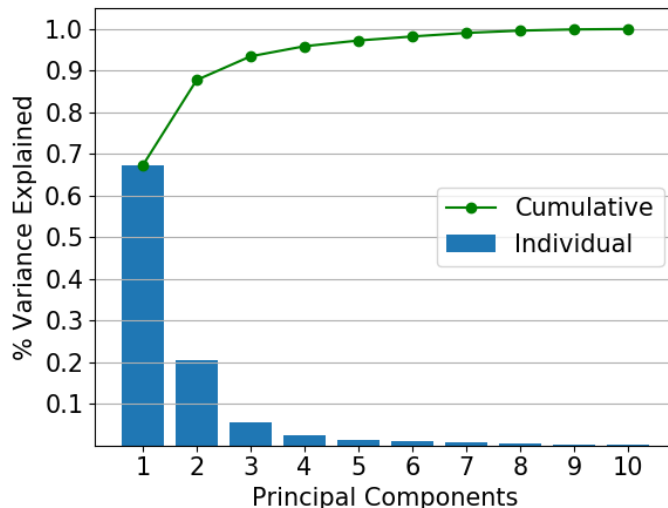


Figure 3.7: Scree plot for principal component analysis using only data from successfully completed manipulation patterns as input.

Appendix C).

It is also clear from Figure 3.8a that the rest pose is well separated from both clusters. Additionally, it should be noted that the rest pose has an outsized influence on the directions of the principal component vectors, since it is repeated eight times in the data. This may seem like an undesirable effect, but it is actually advantageous for our synergies to be able form a very precise reconstruction of the rest pose. This is because, when implementing the synergies in hardware, the rest pose serves as a kind of calibration point, since this is the pose in which the initial positions of each pulley train must be set, such that there is no tension in the tendons, but also very little slack. Therefore, if the reconstruction of the rest pose is inaccurate, this will negatively affect the reconstructions of every other pose.

The hand postures corresponding to the minimum and maximum values of each of the first two PCs are shown in Figure 3.8b. Based on these postures, it seems that each of the first two PCs follow a fairly sensible pattern, and it is not difficult to imagine how they might be used to reconstruct the postures which make up the manipulation patterns in the data. On the other hand, postures from the higher order PCs (shown in Figure 3.9) are much more difficult to make sense of. Nonetheless, they are necessary to properly reconstruct all of the data, and this is part of the power of principal component analysis: the ability to extract useful synergies which could not otherwise be established based solely on human intuition.

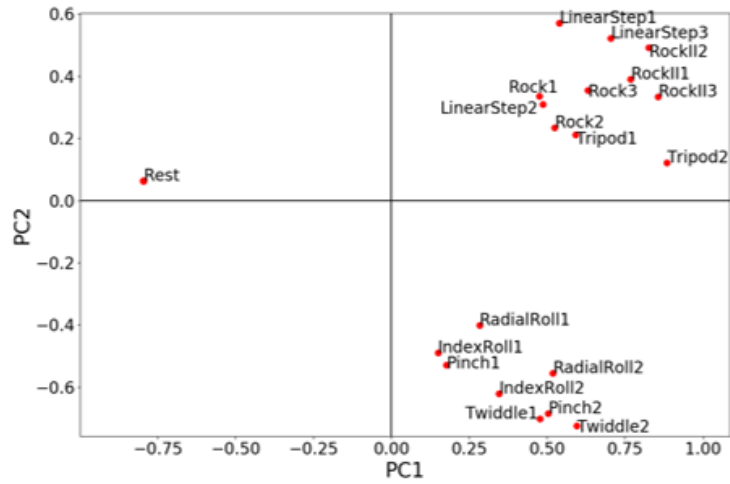
Based on the results from testing with software synergies, we can confidently predict that a mechanical implementation of the first two PCs via pulley trains should enable the hand to achieve 5 of the 13 manipulation patterns from [66], namely Pinch, Dynamic Tripod, RockII, Radial Roll, and Index Roll. Although we cannot claim that this implementation would enable a “high level” of dexterity, it should serve as a promising waypoint for further investigation.

3.3.3 Limitations

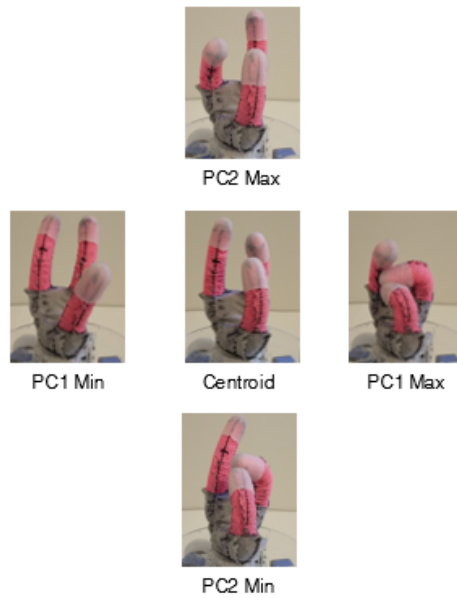
One of the major limitations of this study is the fact that, during testing, the initial contacts between the foam hand and the object being manipulated were always manually adjusted in order to maximize the probability of successfully completing a given pattern. Although this is standard practice for studies involving dexterous manipulation, it may give the impression that the robot is more capable than it actually is. For any ‘real world’ application, a robot would be required to first grasp an object, then (likely) adjust its grasp in order to establish suitable contacts before being able to perform any dexterous manipulation. Having to enable these capabilities greatly increases the difficulty of the dexterous manipulation problem.

Another limitation is that testing of software synergies was limited to only the reconstructed keyframes from the fully actuated tests. In order to properly evaluate each software synergy, they should ideally be exhaustively tested until the full range of postures which they can achieve has been explored. In future studies, this could be accomplished via reinforcement learning.

Finally, the hand prototype itself is substantially limited by its lack of stiffness, as discussed in Section 3.3.1.



(a)



(b)

Figure 3.8: (a) Two-dimensional reconstruction of manipulation patterns. (b) Hand postures corresponding to minimum, maximum, and centroid values for PC1 and PC2.

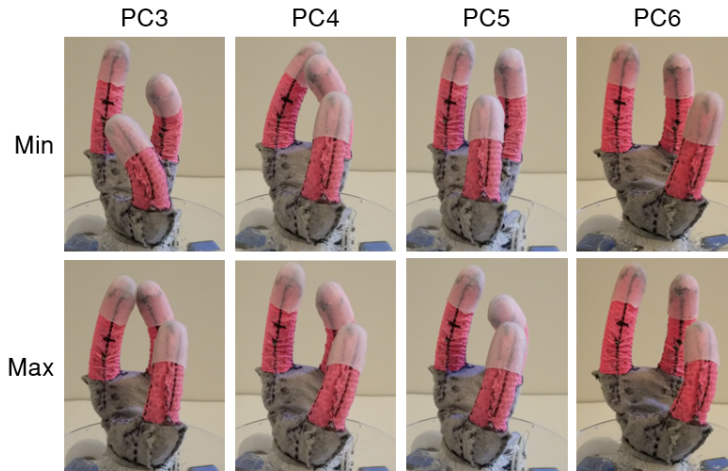


Figure 3.9: Hand postures corresponding to minimum and maximum values of higher order principal components.

3.4 Concluding Remarks

This study involved optimizing the design of a tendon driven foam hand in order to enable a high level of dexterity while requiring a low number (< 5) of motors for actuation. In order to evaluate the dexterity of the hand, a new benchmark test was established based on a manipulation classification from Elliot and Connolly [66]. The optimized hand design consisted of a novel morphology and tendon routing intended to allow for maximal dexterity while using as few tendons as possible. This hand was used - while fully actuated - to perform the established benchmark test, and demonstrated promising levels of dexterity, successfully completing 8 of the 13 manipulation patterns. A principal component analysis was then conducted in order to extract synergies from the data generated during benchmark testing. These synergies were tested in software, and based on the results we concluded that a mechanical implementation would enable the hand to complete 5 of the 13 manipulations from the benchmark test while using only two motors.

Chapter 4

Conclusions and Future Work

This work involved the development of two robotic end effectors, with both designs grounded in the principles of soft robotics. The goal for each end effector was to enable versatile manipulation capabilities while maintaining a simple mechanical design.

The first of these end effectors is a stiffness and adhesion tuning soft gripper. In its soft state, this gripper is highly compliant, and is able to adapt its geometry to objects of varying shapes and sizes, including flat and convex objects. After establishing contact, the gripper transitions to its stiff state, improving load sharing at the contact interface and enabling up to $6\times$ increase in adhesion strength. In this manner, the gripper is able to lift object weighing up to 147 g. In order to release objects, the gripper returns to its soft state, leading to a corresponding decrease in adhesion strength.

This gripper serves as a proof-of-concept for the use of LMPPs in versatile, adhesion based grasping. However, a number of steps must be taken before this gripper can be put to practical use. First, more pull-off data must be collected and the associated final element model must be improved in order to better characterize and understand the adhesion mechanics of the gripper. Additionally, the gripper has several limitations, including a large cycle time, difficulty in releasing lightweight objects, and a limited load capacity, which should all be addressed in future work.

The second end effector developed for this work is a tendon driven foam hand. The entirely soft structure of this hand allows the researcher to easily establish any desired morphology or tendon routing. Accordingly, the design of the hand was optimized in order to enable a high potential for dexterity, while requiring a minimal number of tendons. Additionally, the concept of postural synergies was applied in order to reduce the actuation dimensionality of the hand. Testing with software synergies indicated that the hand could complete 5 distinct dexterous manipulation tasks while using only 2 motors, where each motor drives a pulley train which corresponds to an individual synergy.

This foam hand prototype serves primarily as a waypoint for further investigation. The first step which must be taken in furthering this work is to mechanically implement postural synergies via a

pulley train mechanism. Testing of this implementation will allow for further insight on its design, potentially including a method for implementing more than 2 PCs using pulley trains. Additionally, applying reinforcement learning to control of the hand will likely lead to increased levels of dexterity, and enable more thorough evaluation of different software synergies. Subsequent work may involve applying stiffness tuning architectures to the hand in order to increase its force transmission capability, as well as enabling the hand to operate autonomously, which will require sensorization and planning. It is also likely that the hand design (morphology and tendon routing) selected for this study is not, in fact, an “optimal” design - therefore, different morphologies and tendon routings should also be explored.

To conclude, it is difficult to objectively evaluate whether both of the end effectors developed for this study achieved the stated goal of demonstrating versatile manipulation capabilities while maintaining a simple mechanical design. However, keeping in mind that the ultimate goal is to develop practical end effectors which can be used in “real world” applications, it is clear that both of these end effectors are still in very early stages of development. In fact, most of the main issues associated with soft robotic end effectors - i.e. lack of durability, repeatability, and precision - were not even addressed as a part of this work. For example, we do not know to what extent the adhesive strength of the soft gripper decreases after many uses, or how many cycles can be completed using the foam hand before it experiences a breakage. Therefore, it is important that as research on soft robotic end effectors continues, these important and practical (although perhaps not exciting) considerations are taken into account.

Appendix A

Criteria for Manipulation Patterns

1. **Pinch:** Object is held between two fingers. Both fingers are flexed simultaneously in order to translate the object along the ventro-dorsal axis, towards the palm. Fingers are then simultaneously extended to bring the object back to its starting position.
2. **Dynamic Tripod:** Object is held between three fingers. All three fingers are simultaneously flexed and extended, in repetitive motions, in order to translate the object along the ventro-dorsal axis. Application: writing.
3. **Squeeze:** Deformable object is held between three or more fingers. All fingers are simultaneously flexed towards the object's centroid in order to compress the object, e.g. when squeezing a rubber ball or compressing the plunger of a syringe.
4. **Twiddle:** Object is held between the distal phalanx of one finger (manipulating finger) and along the side of the proximal phalanx of another finger (stabilizing finger). The manipulating finger is flexed and extended in order to roll the object along the length of the stabilizing finger.
5. **Rock:** Round object is held between three or more fingers. Fingers are used to rotate the object about ventro-dorsal axis, e.g. when unscrewing the lid of a bottle.
6. **Rock II:** Elongated object is held in opposed grasp between three fingers. Two of the fingers are alternately flexed and extended in order to pivot the object about the third finger.
7. **Radial Roll:** Object is held between the distal phalanx of one finger (stabilizing finger) and along the side of the proximal phalanx of another finger (manipulating finger). The manipulating finger is flexed and extended in order to roll the object along the length of the stabilizing finger. This pattern is essentially the inverse of Twiddle.
8. **Index Roll:** Object is held between the distal phalanxes of two fingers. One finger is then repetitively flexed and extended in order to roll the object along the length of the other finger.
9. **Full Roll:** Object is held between distal phalanxes of two fingers. One finger is then repet-

itively flexed and extended in order to pivot object about a stationary point on the other finger.


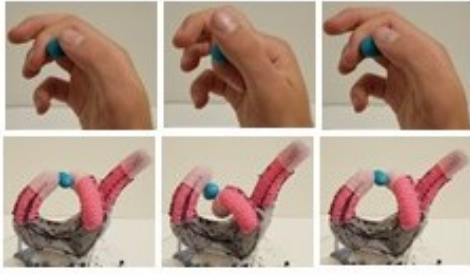

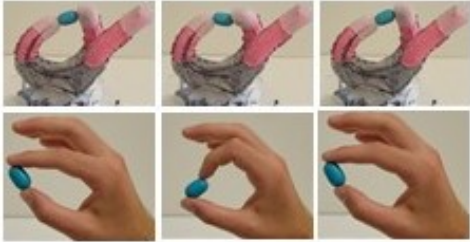

10. **Rotary Step:** Finger-gaiting sequence during which a round object is incrementally rotated about the ventro-dorsal axis by at least 360 degrees.
11. **Interdigital Step:** Finger-gaiting sequence during which an elongated object is incrementally rotated about a pivot point by at least 360 degrees. The rotation occurs about the ventro-dorsal axis.
12. **Linear Step:** Finger-gaiting sequence during which fingers are translated along the length of an elongated object. Sliding between fingers and object is generally required.
13. **Palmar Slide:** Elongated object is held in a palmar grasp. Two fingers, which are initially flexed with their distal phalanxes in contact with the object, are extended in order to translate object along the radio-ulnar axis. Application: removing cap from a pen.

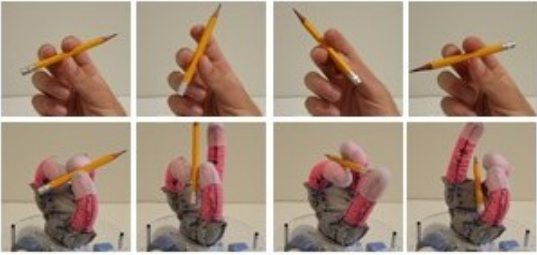


Appendix B

Photo Sequences of Manipulation Patterns

Begins on following page.

Pattern	Categories	Success /Failure	Sequence
Pinch	$\Delta_z(\text{NA})$	Success	     
Dynamic Tripod	$\Delta_z(\text{NA})$	Success	     
Squeeze	$\Delta_y(\text{NA})$	Failure	   
Twiddle	$\Delta_y(A)$ $\theta_z(A)$	Success	     
Rock	$\theta_z(\text{NA})$	Success	       

Pattern	Categories	Success /Failure	Sequence
Rock II	$\theta_z(NA)$	Success	
Radial Roll	$\Delta_y(A)$ $\theta_z(A)$	Success	
Index Roll	$\Delta_z(A)$ $\theta_x(A)$	Success	
Full Roll	$\theta_x(NA)$	Failure	
Rotary Step	$\theta_z(A)$	Failure	

Pattern	Categories	Success /Failure	Sequence
Interdigital Step	$\theta_Y(A)$	Failure	
Linear Step	$\Delta_X(A)$	Success	
Palmar Slide	$\Delta_X(NA)$	Failure	

Appendix C

Low Dimensional Reconstructions of Data

Begins on following page.

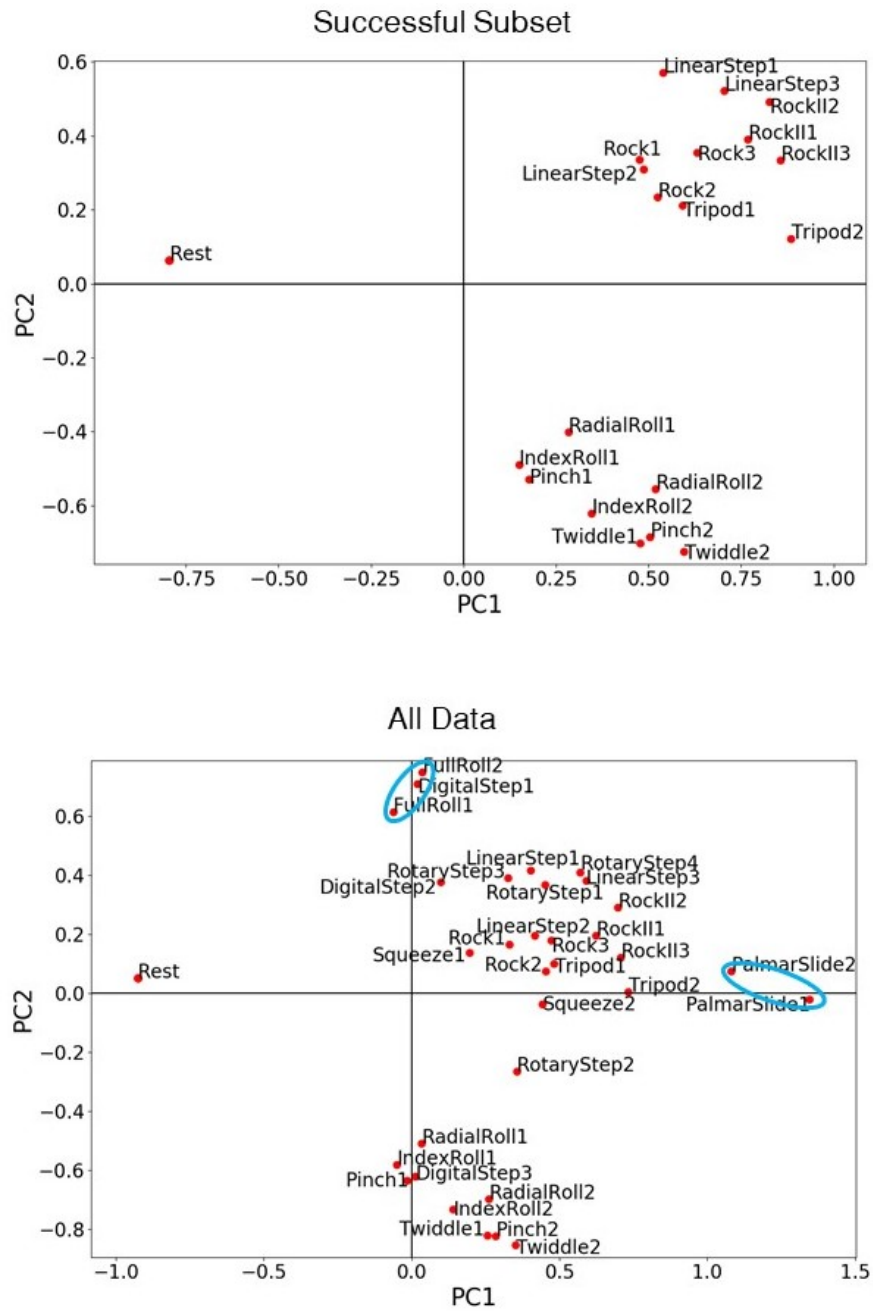


Figure C.1: Two-dimensional reconstructions of manipulation patterns for: (top) successful subset, and (bottom) all data. Clusters not common to both plots are circled in blue.

Appendix D

Dimensioned Drawing of Foam Hand Prototype

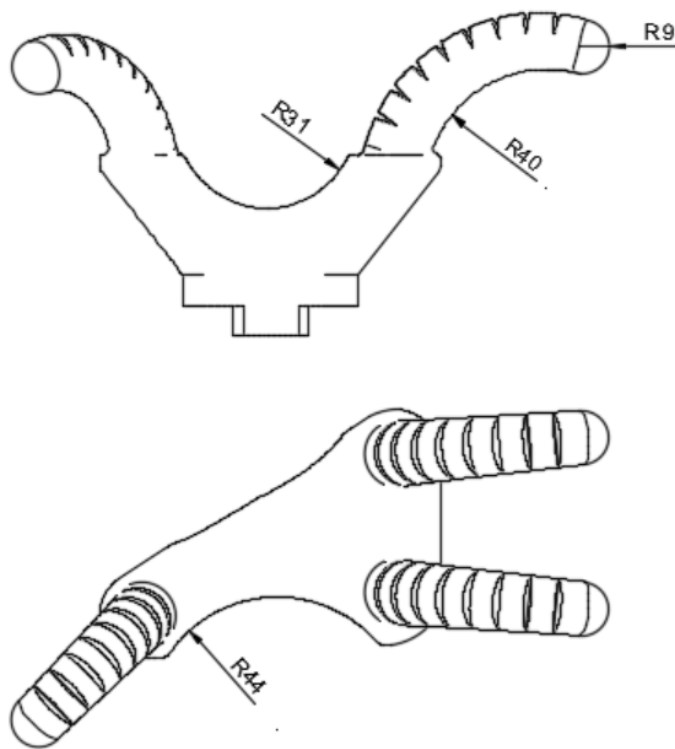


Figure D.1: Dimensions in millimeters. The radius of the base of each finger is 11 mm and the radius of the fingertips is 11 mm. The radius of the mid-line of the index and middle fingers is 50 mm (arc length 79 mm). The radius of the midline of the thumb is 40 mm (arc length 62 mm).

Bibliography

- [1] Steve Jacobsen, E Iversen, D Knutti, R Johnson, and K Biggers. Design of the utah/mit dextrous hand. In *Proceedings. 1986 IEEE International Conference on Robotics and Automation*, volume 3, pages 1520–1532. IEEE, 1986. (document), 1.1, 1.1
- [2] John R Amend, Eric Brown, Nicholas Rodenberg, Heinrich M Jaeger, and Hod Lipson. A positive pressure universal gripper based on the jamming of granular material. *IEEE Transactions on Robotics*, 28(2):341–350, 2012. (document), 1.2, 1.2, 2.1
- [3] Aaron M Dollar and Robert D Howe. The highly adaptive sdm hand: Design and performance evaluation. *The international journal of robotics research*, 29(5):585–597, 2010. (document), 1.2, 1.2
- [4] Raphael Deimel and Oliver Brock. A novel type of compliant and underactuated robotic hand for dexterous grasping. *The International Journal of Robotics Research*, 35(1-3):161–185, 2016. (document), 1.2, 1.2, 3.1
- [5] Elliot W Hawkes, David L Christensen, Amy Kyungwon Han, Hao Jiang, and Mark R Cutkosky. Grasping without squeezing: Shear adhesion gripper with fibrillar thin film. In *2015 IEEE International Conference on Robotics and Automation (ICRA)*, pages 2305–2312. IEEE, 2015. (document), 1.2, 1.2
- [6] C Piazza, G Grioli, MG Catalano, and A Bicchi. A century of robotic hands. *Annual Review of Control, Robotics, and Autonomous Systems*, 2:1–32, 2019. 1.1, 1.1, 3.1
- [7] J Kenneth Salisbury and John J Craig. Articulated hands: Force control and kinematic issues. *The International journal of Robotics research*, 1(1):4–17, 1982. 1.1
- [8] Antonio Bicchi. Hands for dexterous manipulation and robust grasping: A difficult road toward simplicity. *IEEE Transactions on robotics and automation*, 16(6):652–662, 2000. 1.1, 3.1, 3.2.1
- [9] Jun Shintake, Vito Cacucciolo, Dario Floreano, and Herbert Shea. Soft robotic grippers. *Advanced Materials*, 30(29):1707035, 2018. 1.2, 2.1, 3.1
- [10] Rolf Pfeifer, Max Lungarella, and Fumiya Iida. Self-organization, embodiment, and biologically inspired robotics. *Science*, 318(5853):1088–1093, 2007. 1.2
- [11] Eric Brown, Nicholas Rodenberg, John Amend, Annan Mozeika, Erik Steltz, Mitchell R Zakin, Hod Lipson, and Heinrich M Jaeger. Universal robotic gripper based on the jamming of granular material. *Proceedings of the National Academy of Sciences*, 107(44):18809–

18814, 2010. 1.2, 2.1

- [12] Nikolaus Correll, Kostas E Bekris, Dmitry Berenson, Oliver Brock, Albert Causo, Kris Hauser, Kei Okada, Alberto Rodriguez, Joseph M Romano, and Peter R Wurman. Analysis and observations from the first amazon picking challenge. *IEEE Transactions on Automation Science and Engineering*, 15(1):172–188, 2016. 1.2
- [13] Jonathan P King, Dominik Bauer, Cornelia Schlagenhauf, Kai-Hung Chang, Daniele Moro, Nancy Pollard, and Stelian Coros. Design, fabrication, and evaluation of tendon-driven multi-fingered foam hands. In *2018 IEEE-RAS 18th International Conference on Humanoid Robots (Humanoids)*, pages 1–9. IEEE, 2018. 1.3, 3.1, 3.2.3
- [14] Mariangela Manti, Vito Cacucciolo, and Matteo Cianchetti. Stiffening in soft robotics: A review of the state of the art. *IEEE Robotics & Automation Magazine*, 23(3):93–106, 2016. 2.1, 2.2.1
- [15] Liyu Wang, Yang Yang, Yonghua Chen, Carmel Majidi, Fumiya Iida, Erin Askounis, and Qibing Pei. Controllable and reversible tuning of material rigidity for robot applications. *Materials Today*, 21(5):563–576, 2018. 2.1, 2.2.1
- [16] Matteo Cianchetti, Tommaso Ranzani, Giada Gerboni, Iris De Falco, Cecilia Laschi, and Arianna Menciassi. Stiff-flop surgical manipulator: Mechanical design and experimental characterization of the single module. In *2013 IEEE/RSJ international conference on intelligent robots and systems*, pages 3576–3581. IEEE, 2013. 2.1
- [17] Ying Wei, Yonghua Chen, Tao Ren, Qiao Chen, Changxin Yan, Yang Yang, and Yingtian Li. A novel, variable stiffness robotic gripper based on integrated soft actuating and particle jamming. *Soft Robotics*, 3(3):134–143, 2016.
- [18] Kaori Mizushima, Takumi Oku, Yosuke Suzuki, Tokuo Tsuji, and Tetsuyou Watanabe. Multi-fingered robotic hand based on hybrid mechanism of tendon-driven and jamming transition. In *2018 IEEE International Conference on Soft Robotics (RoboSoft)*, pages 376–381. IEEE, 2018. 2.1
- [19] Changyong Cao and Xuanhe Zhao. Tunable stiffness of electrorheological elastomers by designing mesostructures. *Applied Physics Letters*, 103(4):041901, 2013. 2.1
- [20] Anders Pettersson, S Davis, JO Gray, TJ Dodd, and Tomas Ohlsson. Design of a magnetorheological robot gripper for handling of delicate food products with varying shapes. *Journal of Food Engineering*, 98(3):332–338, 2010. 2.1
- [21] Jeffrey D Eisenhaure, Tao Xie, Stephen Varghese, and Seok Kim. Microstructured shape memory polymer surfaces with reversible dry adhesion. *ACS applied materials & interfaces*, 5(16):7714–7717, 2013. 2.1, 2.3.4
- [22] David McCoul, Samuel Rosset, Nadine Besse, and Herbert Shea. Multifunctional shape memory electrodes for dielectric elastomer actuators enabling high holding force and low-voltage multisegment addressing. *Smart Materials and Structures*, 26(2):025015, 2016.
- [23] Wei Wang and Sung-Hoon Ahn. Shape memory alloy-based soft gripper with variable stiffness for compliant and effective grasping. *Soft robotics*, 4(4):379–389, 2017.

- [24] Trevor L Buckner, Edward L White, Michelle C Yuen, R Adam Bilodeau, and Rebecca K Kramer. A move-and-hold pneumatic actuator enabled by self-softening variable stiffness materials. In *2017 IEEE/RSJ International Conference on Intelligent Robots and Systems (IROS)*, pages 3728–3733. IEEE, 2017.
- [25] Yang Yang, Yonghua Chen, Yingtian Li, Zheng Wang, and Yunquan Li. Novel variable-stiffness robotic fingers with built-in position feedback. *Soft robotics*, 4(4):338–352, 2017.
- [26] Amir Firouzeh, Marco Salerno, and Jamie Paik. Stiffness control with shape memory polymer in underactuated robotic origamis. *IEEE Transactions on Robotics*, 33(4):765–777, 2017.
- [27] Yufei Hao, Zemin Liu, Jiaqi Liu, Xi Fang, Shilin Nie, Ying Chun Guan, Tianmiao Wang, Li Wen, et al. A soft gripper with programmable effective length, tactile and curvature sensory feedback. *Smart Materials and Structures*, 2020. 2.1, 2.3.4
- [28] J Krahn, D Sameoto, and C Menon. Controllable biomimetic adhesion using embedded phase change material. *Smart Materials and Structures*, 20(1):015014, 2010. 2.1, 2.2.3, 2.3.1
- [29] Nadia G Cheng, Arvind Gopinath, Lifeng Wang, Karl Iagnemma, and Anette E Hosoi. Thermally tunable, self-healing composites for soft robotic applications. *Macromolecular Materials and Engineering*, 299(11):1279–1284, 2014. 2.1
- [30] Aditya Balasubramanian, Mike Standish, and Christopher J Bettinger. Microfluidic thermally activated materials for rapid control of macroscopic compliance. *Advanced functional materials*, 24(30):4860–4866, 2014. 2.1, 2.3.4
- [31] Liyu Wang, Utku Culha, and Fumiya Iida. A dragline-forming mobile robot inspired by spiders. *Bioinspiration & biomimetics*, 9(1):016006, 2014.
- [32] M Andy McEvoy and Nikolaus Correll. Thermoplastic variable stiffness composites with embedded, networked sensing, actuation, and control. *Journal of Composite Materials*, 49(15):1799–1808, 2015.
- [33] Steven Rich, Sung-Hwan Jang, Yong-Lae Park, and Carmel Majidi. Liquid metal-conductive thermoplastic elastomer integration for low-voltage stiffness tuning. *Advanced Materials Technologies*, 2(12):1700179, 2017.
- [34] Wanliang Shan, Stuart Diller, Abbas Tutcuoglu, and Carmel Majidi. Rigidity-tuning conductive elastomer. *Smart Materials and Structures*, 24(6):065001, 2015.
- [35] Amir Mohammadi Nasab, Amin Sabzehzar, Milad Tatari, Carmel Majidi, and Wanliang Shan. A soft gripper with rigidity tunable elastomer strips as ligaments. *Soft robotics*, 4(4):411–420, 2017. 2.1
- [36] Milad Tatari, Amir Mohammadi Nasab, Kevin T Turner, and Wanliang Shan. Dynamically tunable dry adhesion via subsurface stiffness modulation. *Advanced Materials Interfaces*, 5(18):1800321, 2018. 2.1, 2.2.2, 2.3.1
- [37] Steven I Rich, Vasudevan Nambeesan, Rehan Khan, and Carmel Majidi. Tuning the composition of conductive thermoplastics for stiffness switching and electrically activated healing. *Journal of Intelligent Material Systems and Structures*, 30(18-19):2908–2918, 2019. 2.1,

2.2.1, 2.2.2

- [38] Wanliang Shan, Tong Lu, and Carmel Majidi. Soft-matter composites with electrically tunable elastic rigidity. *Smart Materials and Structures*, 22(8):085005, 2013. 2.1
- [39] Bryan E Schubert and Dario Floreano. Variable stiffness material based on rigid low-melting-point-alloy microstructures embedded in soft poly (dimethylsiloxane)(pdms). *Rsc Advances*, 3(46):24671–24679, 2013.
- [40] Jun Shintake, Bryan Schubert, Samuel Rosset, Herbert Shea, and Dario Floreano. Variable stiffness actuator for soft robotics using dielectric elastomer and low-melting-point alloy. In *2015 IEEE/RSJ International Conference on Intelligent Robots and Systems (IROS)*, pages 1097–1102. IEEE, 2015.
- [41] Ilse M Van Meerbeek, Benjamin C Mac Murray, Jae Woo Kim, Sanlin S Robinson, Perry X Zou, Meredith N Silberstein, and Robert F Shepherd. Morphing metal and elastomer bi-continuous foams for reversible stiffness, shape memory, and self-healing soft machines. *Advanced Materials*, 28(14):2801–2806, 2016. 2.1
- [42] Zhou Ye, Guo Zhan Lum, Sukho Song, Steven Rich, and Metin Sitti. Phase change of gallium enables highly reversible and switchable adhesion. *Advanced Materials*, 28(25):5088–5092, 2016. 2.1
- [43] Sukho Song, Dirk-Michael Drotlef, Carmel Majidi, and Metin Sitti. Controllable load sharing for soft adhesive interfaces on three-dimensional surfaces. *Proceedings of the National Academy of Sciences*, 114(22):E4344–E4353, 2017. 2.2.3, 2.3.4
- [44] Sukho Song, Dirk-M Drotlef, Jamie Paik, Carmel Majidi, and Metin Sitti. Mechanics of a pressure-controlled adhesive membrane for soft robotic gripping on curved surfaces. *Extreme Mechanics Letters*, 30:100485, 2019. 2.1, 2.2.3
- [45] Michael D Bartlett, Eric J Markvicka, and Carmel Majidi. Rapid fabrication of soft, multilayered electronics for wearable biomonitoring. *Advanced Functional Materials*, 26(46):8496–8504, 2016. 2.2.2
- [46] Eric Markvicka, Guanyun Wang, Yi-Chin Lee, Gierad Laput, Carmel Majidi, and Lining Yao. Electrodermis: Fully untethered, stretchable, and highly-customizable electronic bandages. In *Proceedings of the 2019 CHI Conference on Human Factors in Computing Systems*, pages 1–10, 2019. 2.2.2
- [47] Michael D Bartlett and Alfred J Crosby. Scaling normal adhesion force capacity with a generalized parameter. *Langmuir*, 29(35):11022–11027, 2013. 2.2.4
- [48] Michael D Bartlett, Navid Kazem, Matthew J Powell-Palm, Xiaonan Huang, Wenhuan Sun, Jonathan A Malen, and Carmel Majidi. High thermal conductivity in soft elastomers with elongated liquid metal inclusions. *Proceedings of the National Academy of Sciences*, 114(9):2143–2148, 2017. 2.3.4
- [49] Qiguang He, Zhijian Wang, Zhaoqiang Song, and Shengqiang Cai. Bioinspired design of vascular artificial muscle. *Advanced Materials Technologies*, 4(1):1800244, 2019. 2.3.4
- [50] Doh-Gyu Hwang, Katie Trent, and Michael D Bartlett. Kirigami-inspired structures for smart

- adhesion. *ACS applied materials & interfaces*, 10(7):6747–6754, 2018. 2.3.4
- [51] OpenAI: Marcin Andrychowicz, Bowen Baker, Maciek Chociej, Rafal Jozefowicz, Bob McGrew, Jakub Pachocki, Arthur Petron, Matthias Plappert, Glenn Powell, Alex Ray, et al. Learning dexterous in-hand manipulation. *The International Journal of Robotics Research*, 39(1):3–20, 2020. 3.1
- [52] Cosimo Della Santina, Cristina Piazza, Giorgio Grioli, Manuel G Catalano, and Antonio Bicchi. Toward dexterous manipulation with augmented adaptive synergies: The pisa/iit soft-hand 2. *IEEE Transactions on Robotics*, 34(5):1141–1156, 2018. 3.1, 3.2.4, 3.2.4
- [53] Manuel G Catalano, Giorgio Grioli, Edoardo Farnioli, Alessandro Serio, Cristina Piazza, and Antonio Bicchi. Adaptive synergies for the design and control of the pisa/iit soft-hand. *The International Journal of Robotics Research*, 33(5):768–782, 2014. 3.1, 3.2.4, 3.2.4
- [54] Lael U Odhner and Aaron M Dollar. Dexterous manipulation with underactuated elastic hands. In *2011 IEEE International Conference on Robotics and Automation*, pages 5254–5260. IEEE, 2011. 3.1
- [55] Raymond R Ma and Aaron M Dollar. An underactuated hand for efficient finger-gaiting-based dexterous manipulation. In *2014 IEEE International Conference on Robotics and Biomimetics (ROBIO 2014)*, pages 2214–2219. IEEE, 2014.
- [56] Lael U Odhner and Aaron M Dollar. Stable, open-loop precision manipulation with underactuated hands. *The International Journal of Robotics Research*, 34(11):1347–1360, 2015. 3.1, 3.2.1
- [57] Zhe Xu and Emanuel Todorov. Design of a highly biomimetic anthropomorphic robotic hand towards artificial limb regeneration. In *2016 IEEE International Conference on Robotics and Automation (ICRA)*, pages 3485–3492. IEEE, 2016. 3.1
- [58] Cornelia Schlangenhaus, Dominik Bauer, Kai-Hung Chang, Jonathan P King, Daniele Moro, Stelian Coros, and Nancy Pollard. Control of tendon-driven soft foam robot hands. In *2018 IEEE-RAS 18th International Conference on Humanoid Robots (Humanoids)*, pages 1–7. IEEE, 2018. 3.1
- [59] Dominik Bauer, Cornelia Bauer, Jonathan P King, Daniele Moro, Kai-Hung Chang, Stelian Coros, and Nancy Pollard. Design and control of foam hands for dexterous manipulation. *International Journal of Humanoid Robotics*, 17(01):1950033, 2020. 3.1
- [60] Marco Santello, Martha Flanders, and John F Soechting. Postural hand synergies for tool use. *Journal of neuroscience*, 18(23):10105–10115, 1998. 3.1, 3.2.4
- [61] Ian M Bullock, Raymond R Ma, and Aaron M Dollar. A hand-centric classification of human and robot dexterous manipulation. *IEEE transactions on Haptics*, 6(2):129–144, 2012. 3.2.1
- [62] A Kapandji. Clinical test of apposition and counter-apposition of the thumb. *Annales de chirurgie de la main: organe officiel des sociétés de chirurgie de la main*, 5(1):67, 1986. 3.2.1
- [63] Erika Davis Sears and Kevin C Chung. Validity and responsiveness of the jebesen–taylor hand function test. *The Journal of hand surgery*, 35(1):30–37, 2010. 3.2.1

- [64] Justine Desrosiers, R Hebert, G Bravo, and E Dutil. The purdue pegboard test: normative data for people aged 60 and over. *Disability and rehabilitation*, 17(5):217–224, 1995. 3.2.1
- [65] Liz Haverkate, Gerwin Smit, and Dick H Plettenburg. Assessment of body-powered upper limb prostheses by able-bodied subjects, using the box and blocks test and the nine-hole peg test. *Prosthetics and orthotics international*, 40(1):109–116, 2016. 3.2.1
- [66] John M Elliott and KJ Connolly. A classification of manipulative hand movements. *Developmental Medicine & Child Neurology*, 26(3):283–296, 1984. 3.2.1, 3.2.2, 3.2.3, 3.2.4, 3.3.1, 3.3.2, 3.4
- [67] Christopher Y Brown and H Harry Asada. Inter-finger coordination and postural synergies in robot hands via mechanical implementation of principal components analysis. In *2007 IEEE/RSJ International Conference on Intelligent Robots and Systems*, pages 2877–2882. IEEE, 2007. 3.2.4, 3.2.4
- [68] Wenbin Chen, Caihua Xiong, and Shigang Yue. Mechanical implementation of kinematic synergy for continual grasping generation of anthropomorphic hand. *IEEE/ASME Transactions on Mechatronics*, 20(3):1249–1263, 2014. 3.2.4
- [69] Shunchong Li, Xinjun Sheng, Honghai Liu, and Xiangyang Zhu. Design of a myoelectric prosthetic hand implementing postural synergy mechanically. *Industrial Robot: An International Journal*, 2014. 3.2.4
- [70] Giulia C Matrone, Christian Cipriani, Emanuele L Secco, Giovanni Magenes, and Maria Chiara Carrozza. Principal components analysis based control of a multi-dof underactuated prosthetic hand. *Journal of neuroengineering and rehabilitation*, 7(1):1–13, 2010. 3.2.4, 3.2.4
- [71] Hervé Abdi and Lynne J Williams. Principal component analysis. *Wiley interdisciplinary reviews: computational statistics*, 2(4):433–459, 2010. 3.2.4
- [72] Lionel Birglen, Thierry Laliberté, and Clément M Gosselin. *Underactuated robotic hands*, volume 40. Springer, 2007. 3.2.4
- [73] Thierry Laliberté, Mathieu Baril, François Guay, and Clément Gosselin. Towards the design of a prosthetic underactuated hand. *Mechanical Sciences*, 1(1):19–26, 2010.
- [74] Raymond R Ma, Lael U Odhner, and Aaron M Dollar. A modular, open-source 3d printed underactuated hand. In *2013 IEEE International Conference on Robotics and Automation*, pages 2737–2743. IEEE, 2013. 3.2.4